



Ab initio study of electromagnetic modes in two-dimensional semiconductors: Application to doped phosphorene

Dino Novko ^{1,2}, Keenan Lyon,^{3,4} Duncan J. Mowbray,⁵ and Vito Despoja ^{1,2}

¹*Institute of Physics, 10000 Zagreb, Croatia*

²*Donostia International Physics Center (DIPC), 20018 San Sebastián, Spain*

³*Department of Applied Mathematics, University of Waterloo, Waterloo, Ontario, Canada*

⁴*Department of Physics and Astronomy, Uppsala University, S-751 20, Uppsala, Sweden*

⁵*School of Physical Sciences and Nanotechnology, Yachay Tech University, Urcuqui 100119, Ecuador*



(Received 9 June 2021; revised 10 August 2021; accepted 7 September 2021; published 17 September 2021)

Starting from the rigorous quantum-field-theory formalism, we derive a formula for the screened conductivity designed to study the coupling of light with elementary electron excitations and the ensuing electromagnetic modes in two-dimensional (2D) semiconductors. The latter physical quantity consists of three fully separable parts, namely, intraband, interband, and ladder conductivities, and is calculated beyond the random phase approximation as well as from first principles. By using this methodology, we study the optical absorption spectra in 2D black phosphorous, so-called phosphorene, as a function of the concentration of electrons injected into the conduction band. The mechanisms of phosphorene exciton quenching versus doping are studied in detail. It is demonstrated that already small doping levels ($n \sim 10^{12} \text{ cm}^{-2}$) lead to a radical drop in the exciton binding energy, i.e., from 600 meV to 128 meV. The screened conductivity is applied to study the collective electromagnetic modes in doped phosphorene. It is shown that the phosphorene transversal exciton hybridizes with free photons to form an exciton-polariton. This phenomenon is experimentally observed only for the case of confined electromagnetic microcavity modes. Finally, we demonstrate that the energy and intensity of anisotropic 2D plasmon-polaritons can be tuned by varying the concentration of injected electrons.

DOI: [10.1103/PhysRevB.104.115421](https://doi.org/10.1103/PhysRevB.104.115421)

I. INTRODUCTION

Semiconducting two-dimensional (2D) crystals became very attractive in terms of their very interesting optical and electromagnetic properties. Transition metal dichalcogenides (TMDs) support tunable [1,2] and strong excitons or exciton-polaritons [3] in the visible frequency range [4,5], which can potentially be applied in various optoelectronic devices [6]. Increasing attention has also been given to excitons and trions affected by the dielectric environment [7]. Important as well for our understanding of light-matter interaction are the studies of strong hybridization between TMD excitons and dielectric microcavity photons that results in the formation of exciton-polariton modes [8–12]. In addition, doped 2D semiconductors can support collective electron excitation modes known as plasmons [13–15], with promising applications as reported in TMDs/graphene and in gold heterostructures [16,17]. Recently, a class of 2D materials has emerged that supports anisotropic electromagnetic modes [18]. The most famous anisotropic 2D crystal is a single layer of black phosphorus, also known as phosphorene, which supports tunable 2D hyperbolic plasmon [19].

The optical properties and dielectric response of phosphorene have been systematically investigated [13,19–38]. For instance, the intensities and tuning of hyperbolic plasmons in supported or self-standing phosphorene were explored by using different models for the optical conductivity, either via

tight binding approximation (TBA) fitted to density functional theory (DFT) calculations or via electron self-energy approximation GW [13,19,21]. Also, optical properties, including optical reflection, transmission, absorption, and plasmon-polaritons in phosphorene, were studied in great detail by means of the TBA optical conductivity tensor [22,23]. Optical properties of multilayer phosphorene as a function of the number of layers (thickness) [38], doping, and light polarization [25] were explored. Further, the electron energy loss spectra and anisotropic plasmons in phosphorene were studied by means of *ab initio* techniques [26,27]. Besides the hyperbolic plasmon, phosphorene shows very interesting excitonic effects. Sophisticated GW-BSE (GW approximation which includes solving the Bethe-Salpeter equation) calculations of the quasiparticle band gap and exciton binding energies as a function of strain, polarization, and dielectric environment were studied in phosphorene [28–33]. Moreover, the excitonic fine structure in monolayer and few-layer black phosphorus were studied through reflection and photoluminescence excitation measurements [35]. In Refs. [36,37], anisotropic photoluminescence, the quasiparticle band gap, and the exciton binding energy in phosphorene were studied and compared with theoretical calculations.

These extensive studies have shown that electromagnetic excitations (i.e., plasmon-polaritons and exciton-polaritons) in pristine and doped phosphorene crystals display remarkable optical properties. In this paper, we derive a

compact formula for the investigation of electromagnetic modes in 2D crystals, where the optical conductivity tensor $\sigma_{\mu\nu}(\omega) = \sigma_{\mu\nu}^{\text{intra}}(\omega) + \sigma_{\mu\nu}^{\text{inter}}(\omega) + \sigma_{\mu\nu}^{\text{ladd}}(\omega)$ is the only input expression and is fully calculated from first principles. The first two terms $\sigma^{\text{RPA}} = \sigma^{\text{intra}} + \sigma^{\text{inter}}$ represent the random phase approximation (RPA), while the third term σ^{ladd} represents the ladder contribution to the optical conductivity. In tandem, this becomes the RPA + ladder approximation. This approach is completely analogous to the widely used GW-BSE method [39–46], which is commonly utilized to calculate the quasiparticle and optical properties of various 2D semiconductors [4,5,47–51], including phosphorene [28,29,36,38]. The RPA + ladder approximation allows for RPA and ladder terms to be calculated independently, so the RPA contribution can be calculated at the required higher level of accuracy (using many bands and dense \mathbf{K} -point meshes), while the computationally demanding ladder contribution can be calculated by using fewer bands and a coarser \mathbf{K} -point grid. This could significantly reduce the computational cost while including excitonic effects to a moderate level of accuracy. This is usually not the case in the standard BSE calculations where the Hartree (RPA) and Fock (ladder) BSE kernels form a two-particle Hamiltonian (single matrix in energy-momentum space) [47] and must be calculated at the same level of accuracy. Also, here the RPA conductivity is further separated into σ^{intra} (Drude intraband) and to σ^{inter} (interband) terms, which facilitates analysis of doped semiconductors. In this paper, the RPA + ladder approximation will be applied to study two kinds of electromagnetic modes in doped phosphorene, namely, plasmon- and exciton-polaritons.

The paper is organized as follows. In Sec. II, we present the derivation of the optical conductivity $\sigma_{\mu}(\omega)$ in the RPA + ladder approximation along with the solution of the Dyson equation for the electric field $E_{\mu}(\mathbf{Q}, \omega)$ in the vicinity of a 2D crystal. In Sec. III, we demonstrate how the injection of electrons into the phosphorene conduction band (extra electronic screening $\Delta W = W_0^{\text{dop}} - W_0^0$) influences the principal exciton intensity and binding energy, present results showing the hybridization between the exciton and free photons (i.e., formation of exciton-polaritons), and, finally, show the RPA optical conductivities $\sigma^{\text{RPA}} = \sigma^{\text{intra}} + \sigma^{\text{inter}}$, the effective number of in-plane charge carriers $n_{\mu}^{e,h}$, and the intensities of plasmon-polaritons in doped phosphorene. The conclusions are presented in Sec. IV.

II. THEORETICAL FORMULATION

The system we explore consists of electrons which move within the effective crystal potential and which interact with free photons so the total Hamiltonian of the system can be written as

$$H = H_{\text{el}} + H_{\text{ph}} + H_{\text{el-ph}}. \quad (1)$$

Here

$$H_{\text{el}} = \sum_{n\mathbf{K}} E_{n\mathbf{K}} c_{n\mathbf{K}}^{\dagger} c_{n\mathbf{K}} \quad (2)$$

represents the electrons which move in the effective Kohn-Sham (KS) potential. The $c_{n\mathbf{K}}^{\dagger}/c_{n\mathbf{K}}$ are the creation/annihilation operators of an electron in Bloch

state $|n, \mathbf{K}\rangle$ represented by the wave function $\phi_{n\mathbf{K}}$ and energy $E_{n\mathbf{K}}$, where n is the band index and $\mathbf{K} = (K_x, K_y)$ parallel wave vector. Analogously,

$$H_{\text{ph}} = \sum_{\mu\mathbf{q}} \hbar |\mathbf{q}| c \left\{ a_{\mu\mathbf{q}}^{\dagger} a_{\mu\mathbf{q}} + \frac{1}{2} \right\} \quad (3)$$

represents the free photons, where $a_{\mu\mathbf{q}}^{\dagger}/a_{\mu\mathbf{q}}$ are the creation/annihilation operators of a photon with polarization μ , \mathbf{q} is a three-dimensional (3D) wave vector, and c is the speed of light. In the $\Phi = 0$ gauge, the part of the Hamiltonian which represents the interaction between electrons and photons can be written as [52,53]

$$H_{\text{el-ph}} = -\frac{1}{c} \int d^3\mathbf{r} \mathbf{j} \cdot \mathbf{A} + \frac{e^2}{2mc^2} \int d^3\mathbf{r} \rho \mathbf{A}^2. \quad (4)$$

Here, \mathbf{A} is the electromagnetic field or vector potential operator, the fermionic current operator is

$$\mathbf{j} = \frac{e\hbar}{2im} \{\Psi^{\dagger} \nabla \Psi - [\nabla \Psi^{\dagger}] \Psi\}, \quad (5)$$

the fermionic density operator is defined as

$$\rho = \Psi^{\dagger} \Psi,$$

and the fermionic field operator is

$$\psi(\mathbf{r}) = \sum_{n,\mathbf{K}} \phi_{n\mathbf{K}}(\mathbf{r}) c_{n\mathbf{K}}. \quad (6)$$

We emphasize here that the spin quantum number $s = \pm 1/2$ will be merged with the band's quantum number, i.e., $n \equiv (n, s)$. The time-ordered photon propagator is defined as

$$D_{\mu\nu}(\mathbf{r}, \mathbf{r}'; t - t') = \frac{i}{\hbar c} \langle \Phi_0 | T \{ A_{\mu}(\mathbf{r}, t) A_{\nu}(\mathbf{r}', t') \} | \Phi_0 \rangle, \quad (7)$$

where T represents the time ordering operator, $A_{\mu}(t) = e^{iHt/\hbar} A_{\mu}(t=0) e^{-iHt/\hbar}$ is the Heisenberg operator, and $|\Phi_0\rangle$ is a ground state of the total Hamiltonian in Eq. (1). After employing the standard perturbation theory method for the boson Green's functions [52–54], it can be shown that the photon propagator in Eq. (7) satisfies the Dyson equation

$$\begin{aligned} D_{\mu\nu}(\mathbf{r}, \mathbf{r}', \omega) &= D_{\mu\nu}^0(\mathbf{r}, \mathbf{r}', \omega) + \sum_{\alpha, \beta=1}^3 \int d^2\rho_1 \int_{-L/2}^{L/2} dz_1 \int d^2\rho_2 \int_{-L/2}^{L/2} dz_2 \\ &\quad \times D_{\mu\alpha}^0(\mathbf{r}, \mathbf{r}_1, \omega) \Pi_{\alpha\beta}(\mathbf{r}_1, \mathbf{r}_2, \omega) D_{\beta\nu}(\mathbf{r}_2, \mathbf{r}', \omega), \end{aligned} \quad (8)$$

which is also illustrated with Feynman diagrams in Fig. 1(a). Here the free-photon propagator is

$$D_{\mu\nu}^0(\mathbf{r}, \mathbf{r}'; t - t') = \frac{i}{\hbar c} \langle \Phi_0^{\text{ph}} | T \{ A_{\mu}(\mathbf{r}, t) A_{\nu}(\mathbf{r}', t') \} | \Phi_0^{\text{ph}} \rangle, \quad (9)$$

where $A_{\mu}(t) = e^{iH_{\text{ph}}t/\hbar} A_{\mu}(t=0) e^{-iH_{\text{ph}}t/\hbar}$ is the interaction picture operator and $|\Phi_0^{\text{ph}}\rangle$ is the photonic vacuum or ground state of a free-photon Hamiltonian [see Eq. (3)]. In this paper, we restrict ourselves to the RPA + ladder approximation such that the photon self-energy Π consists of two terms, i.e.,

$$\Pi_{\alpha\beta}(\mathbf{r}, \mathbf{r}', \omega) = \Pi_{\alpha\beta}^{\text{RPA}}(\mathbf{r}, \mathbf{r}', \omega) + \Pi_{\alpha\beta}^{\text{ladd}}(\mathbf{r}, \mathbf{r}', \omega), \quad (10)$$

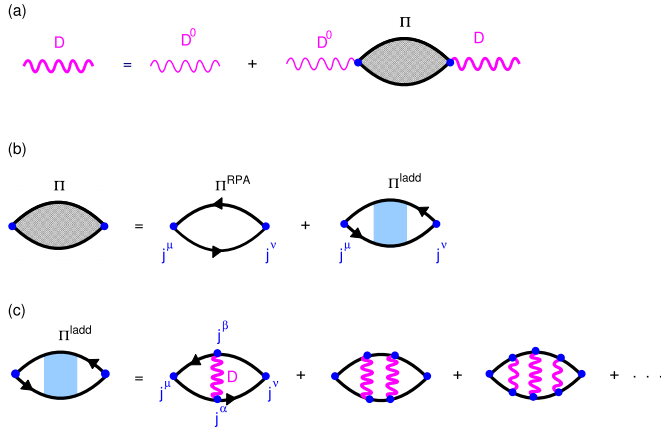


FIG. 1. (a) Feynman diagrams representing the Dyson equation in Eq. (8). (b) Photon self-energy in the RPA + ladder approximation. (c) Perturbative expansion of the ladder photon self-energy Π^{ladder} . Blue dots represent the current vertices j^μ , black lines are single-particle time-ordered Green's functions G , and thin and thick magenta wavy lines represent the bare $D_{\mu\nu}^0$ and the screened $D_{\mu\nu}$ photon propagators, respectively.

where the first RPA, and the second ladder contributions are illustrated by Feynman diagrams in Figs. 1(b) and 1(c). It should be noted that in Eq. (8), the integration is restricted within the volume of the supercell $z \in [-L/2, L/2]$ (as shown in Fig. 2) which cancels the spurious intersupercell electron-electron interactions.

In what follows, the methodology used to solve the Dyson equation in Eq. (8) is shown with an emphasis on the calculation of the ladder photon self-energy, while the detailed derivation of the RPA photon self-energy is in Ref. [53]. Considering that the crystal super-lattice is periodic in 3D, all

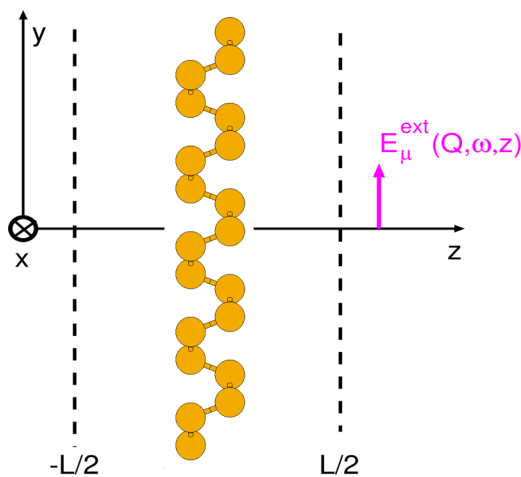


FIG. 2. Geometry of the system. The 2D crystal (in this case, phosphorene) represents one supercell which periodically repeats in the perpendicular z direction, where L represents the supercell constant in that direction. The volume integration in Eq. (8) is restricted within a volume of one supercell $z \in [-L/2, L/2]$, which means that the photons can interact solely with the Bloch electrons in the corresponding supercell

tensors can be Fourier expanded as

$$T_{\alpha\beta}(\mathbf{r}, \mathbf{r}', \omega) = \frac{1}{L} \sum_{\mathbf{G}\mathbf{G}'} \int \frac{d\mathbf{Q}}{(2\pi)^2} e^{i(\mathbf{Q}+\mathbf{G})\mathbf{r}} e^{-i(\mathbf{Q}+\mathbf{G}')\mathbf{r}'} \times T_{\alpha\beta\mathbf{G}\mathbf{G}'}(\mathbf{Q}, \omega), \quad (11)$$

where $\mathbf{Q} = (Q_x, Q_y)$ is the momentum transfer wave-vector parallel to the $x-y$ plane, $\mathbf{G} = (\mathbf{G}_\parallel, G_z)$ are 3D reciprocal lattice vectors, and $\mathbf{r} = (\boldsymbol{\rho}, z)$ is a 3D position vector. After using Eq. (11), the Dyson equation transforms into the matrix equation:

$$D_{\mu\nu, \mathbf{G}\mathbf{G}'}(\mathbf{Q}, \omega) = D_{\mu\nu, \mathbf{G}\mathbf{G}'}^0(\mathbf{Q}, \omega) + \sum_{\alpha\beta, \mathbf{G}_1\mathbf{G}_2} D_{\mu\alpha, \mathbf{G}\mathbf{G}_1}^0(\mathbf{Q}, \omega) \times \Pi_{\alpha\beta, \mathbf{G}_1\mathbf{G}_2}(\mathbf{Q}, \omega) D_{\beta\nu, \mathbf{G}_2\mathbf{G}'}(\mathbf{Q}, \omega). \quad (12)$$

The 3D Fourier transform of the free-photon propagator becomes

$$\mathbf{D}_{\mathbf{G}, \mathbf{G}'}^0(\mathbf{Q}, \omega) = \frac{1}{L} \delta_{\mathbf{G}\mathbf{G}'} \int_{-L/2}^{L/2} e^{-iG_z z} \times \mathbf{D}^0(\mathbf{Q} + \mathbf{G}_\parallel, \omega, z, z') e^{iG_z' z'} dz dz', \quad (13)$$

where the partial Fourier transform of the free-photon propagator in the $x-y$ plane is explicitly [52]

$$\mathbf{D}^0(\mathbf{Q}, \omega, z, z') = -\frac{4\pi c}{\omega^2} \delta(z-z') \mathbf{z} \cdot \mathbf{z} + \frac{2\pi i}{c\beta} \{\mathbf{e}_s \cdot \mathbf{e}_s + \mathbf{e}_p \cdot \mathbf{e}_p\} e^{i\beta|z-z'|}. \quad (14)$$

Here the unit vectors are adapted to the geometry of the system such that $\mathbf{e}_s = \mathbf{Q}_0 \times \mathbf{z}$ and $\mathbf{e}_p = \frac{c}{\omega} [-\beta \text{sgn}(z-z') \mathbf{Q}_0 + Q\mathbf{z}]$ (where \mathbf{Q}_0 is the unit vector in the \mathbf{Q} direction) represent directions of s(TE) and p(TM) polarized fields, respectively. The complex wave vector in the perpendicular (z) direction is defined as $\beta = \sqrt{\frac{\omega^2}{c^2} - Q^2}$.

The Fourier transform of the photon self-energy is

$$\Pi_{\mu\nu, \mathbf{G}\mathbf{G}'}(\mathbf{Q}, \omega) = \Pi_{\mu\nu, \mathbf{G}\mathbf{G}'}^{\text{RPA}}(\mathbf{Q}, \omega) + \Pi_{\mu\nu, \mathbf{G}\mathbf{G}'}^{\text{ladder}}(\mathbf{Q}, \omega), \quad (15)$$

where the RPA photon self-energy is explicitly [53]

$$\Pi_{\mu\nu, \mathbf{G}\mathbf{G}'}^{\text{RPA}}(\mathbf{Q}, \omega) = \frac{1}{\Omega c} \sum_{nm\mathbf{K}} \frac{\hbar\omega}{E_{n\mathbf{K}} - E_{m\mathbf{K}+\mathbf{Q}}} \times \frac{f_{n\mathbf{K}} - f_{m\mathbf{K}+\mathbf{Q}}}{\hbar\omega + i\eta + E_{n\mathbf{K}} - E_{m\mathbf{K}+\mathbf{Q}}} \times j_{n\mathbf{K}, m\mathbf{K}+\mathbf{Q}}^\mu(\mathbf{G}) [j_{n\mathbf{K}, m\mathbf{K}+\mathbf{Q}}^\nu(\mathbf{G}')]^*, \quad (16)$$

where $\Omega = S \times L$ is the normalization volume, S is the normalization surface, and $f_{n\mathbf{K}} = [e^{(E_{n\mathbf{K}} - E_F)/kT} + 1]^{-1}$ is the Fermi-Dirac distribution function at the temperature T . The current vertices are defined as

$$j_{n\mathbf{K}, m\mathbf{K}+\mathbf{Q}}^\alpha(\mathbf{G}) = \int_{\Omega} d\mathbf{r} e^{-i(\mathbf{Q}+\mathbf{G})\mathbf{r}} j_{n\mathbf{K}, m\mathbf{K}+\mathbf{Q}}^\alpha(\mathbf{r}), \quad (17)$$

and the current $j_{n\mathbf{K}, m\mathbf{K}+\mathbf{Q}}^\alpha(\mathbf{r})$ produced by transition between Bloch states $|n\mathbf{K}\rangle \rightarrow |m\mathbf{K}+\mathbf{Q}\rangle$ is equal to

$$\frac{e\hbar}{2im} \{\phi_{n\mathbf{K}}^*(\mathbf{r}) \partial_\alpha \phi_{m\mathbf{K}+\mathbf{Q}}(\mathbf{r}) - [\partial_\alpha \phi_{n\mathbf{K}}^*(\mathbf{r})] \phi_{m\mathbf{K}+\mathbf{Q}}(\mathbf{r})\}.$$

Note that we use the current-current formalism with the current matrix elements to construct the optical conductivity formulas, which is slightly different from the common formalism based on the velocity operators and matrix elements. The advantage of using the current matrix elements is that there are no nonlocal contributions to the matrix elements coming from the nonlocal part of the pseudopotentials [55].

The ladder photon self-energy is

$$\begin{aligned} \Pi_{\mu\nu, \mathbf{G}\mathbf{G}'}^{\text{ladd}}(\mathbf{Q}, \omega) = & -\frac{1}{\Omega c} \sum_{nm\mathbf{K}} \sum_{n'm'\mathbf{K}'} j_{n\mathbf{K}, m\mathbf{K}+\mathbf{Q}}^{\mu}(\mathbf{G}) \\ & \times \mathcal{K}_{n\mathbf{K} \rightarrow n'\mathbf{K}'}^{m\mathbf{K}+\mathbf{Q} \leftarrow m'\mathbf{K}'+\mathbf{Q}}(\omega) [j_{n'\mathbf{K}', m'\mathbf{K}'+\mathbf{Q}}^{\nu}(\mathbf{G}')]^*, \end{aligned} \quad (18)$$

where the ladder four-point polarizability \mathcal{K} can be obtained by solving the matrix equation in $\{\mathbf{K}, n\}$ space,

$$\mathcal{K}^{\text{ladd}}(\omega) = \mathcal{L}(\omega) \otimes \Xi^F \otimes \mathcal{L}(\omega) + \mathcal{L}(\omega) \otimes \Xi^F \otimes \mathcal{K}^{\text{ladd}}(\omega), \quad (19)$$

where matrix multiplication represents summation over the bands and wave vectors as $\otimes \equiv \sum_{nm} \sum_{\mathbf{K}}$. Here the time-ordered electron-hole propagator is defined as

$$\mathcal{L}_{n\mathbf{K} \rightarrow n'\mathbf{K}'}^{m\mathbf{K}+\mathbf{Q} \leftarrow m'\mathbf{K}'+\mathbf{Q}} = \int_{-\infty}^{\infty} \frac{d\omega'}{2\pi i} G_{n\mathbf{K}}(\omega') G_{m\mathbf{K}+\mathbf{Q}}(\omega + \omega'). \quad (20)$$

In the quasiparticle approximation (long lifetime approximation), the time-ordered single-particle propagator is defined as

$$G_{n\mathbf{K}}(\omega) = \frac{1 - f_{n\mathbf{K}}}{\omega - E_{n\mathbf{K}} + i\eta} + \frac{f_{n\mathbf{K}}}{\omega - E_{n\mathbf{K}} - i\eta}, \quad (21)$$

where the single-particle energies $E_{n\mathbf{K}}$ are calculated by combining DFT and quasiparticle GW corrections [43]. After substituting Eq. (21) into Eq. (20), the time-ordered electron-hole propagator becomes explicitly

$$\begin{aligned} \mathcal{L}_{n\mathbf{K} \rightarrow n'\mathbf{K}'}^{m\mathbf{K}+\mathbf{Q} \leftarrow m'\mathbf{K}'+\mathbf{Q}} = & \delta_{nn'} \delta_{mm'} \delta_{\mathbf{K}\mathbf{K}'} \left\{ \frac{f_{n\mathbf{K}}(1 - f_{m\mathbf{K}+\mathbf{Q}})}{\omega + E_{n\mathbf{K}} - E_{m\mathbf{K}+\mathbf{Q}} + i\delta} \right. \\ & \left. - \frac{f_{m\mathbf{K}+\mathbf{Q}}(1 - f_{n\mathbf{K}})}{\omega + E_{n\mathbf{K}} - E_{m\mathbf{K}+\mathbf{Q}} - i\delta} \right\}. \end{aligned} \quad (22)$$

The photonic Bethe-Salpeter-Fock kernel is

$$\begin{aligned} \Xi_{n\mathbf{K} \rightarrow n'\mathbf{K}'}^{F, m\mathbf{K}+\mathbf{Q} \leftarrow m'\mathbf{K}'+\mathbf{Q}} = & -\frac{1}{\Omega c} \sum_{\mu\nu} \sum_{\mathbf{G}_1 \mathbf{G}_2} [j_{n\mathbf{K}, n'\mathbf{K}'}^{\mu}(\mathbf{G}_1)]^* \\ & \times [-D_{\mathbf{G}_1 \mathbf{G}_2}^{\text{RPA}, \mu\nu}(\mathbf{K}' - \mathbf{K}, \Delta\omega \approx 0)] \\ & \times j_{m\mathbf{K}+\mathbf{Q}, m'\mathbf{K}'+\mathbf{Q}}^{\nu}(\mathbf{G}_2). \end{aligned} \quad (23)$$

Here, the RPA photon propagator $D^{\text{RPA}, \mu\nu}$ is the solution of the Dyson equation [see Eq. (12)] for $\Pi_{\mu\nu} = \Pi_{\mu\nu}^{\text{RPA}}$, which is explicitly defined in Ref. [16]. The photonic Fock-kernel in Eq. (23) represents scattering between excited electrons and holes mediated by the photon propagator $D_{\mu\nu}$, as sketched in Fig. 3(a) and in the Feynman diagram in Fig. 3(b). Considering that the average electron-hole distance or average exciton radius satisfies $r_{\text{ex}} \ll c/\Delta\omega$, where $\Delta\omega \approx \hbar^2(\mathbf{K}'^2 - \mathbf{K}^2)/2m_{e,h}$ is electron or hole scattering frequency [as sketched in Fig. 3(a)], the interaction between electrons and holes mediated by radiative electromagnetic modes (the excitonic Lamb

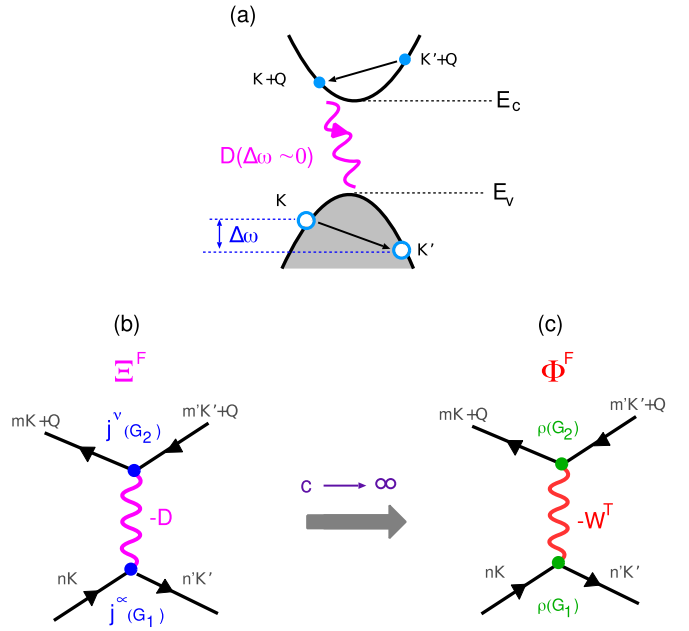


FIG. 3. (a) The electron hole scattering mediated by the photon propagator $D_{\mu\nu}$. (b) The Feynman diagram for the photonic Bethe-Salpeter-Fock kernel in Eq. (23). (c) In the nonretarded limit ($c \rightarrow \infty$), the photonic Fock kernel Ξ^F becomes the standard Fock kernel Φ^F in Eq. (24), which represents the electron-hole scattering mediated by screened Coulomb interaction W^T .

shift) is negligible, and in Ξ^F we can omit electromagnetic retardation effects. This effectively implies that the propagator $D^{\mu\nu}$ can be reduced to the screened Coulomb interaction W^T such that the current vertices j^μ become charge vertices ρ and the photon-Fock kernel transforms as

$$\begin{aligned} \lim_{c \rightarrow \infty} \Xi_{n\mathbf{K} \rightarrow n'\mathbf{K}'}^{F, m\mathbf{K}+\mathbf{Q} \leftarrow m'\mathbf{K}'+\mathbf{Q}} = & \Phi_{n\mathbf{K} \rightarrow n'\mathbf{K}'}^{F, m\mathbf{K}+\mathbf{Q} \leftarrow m'\mathbf{K}'+\mathbf{Q}}(\omega) \\ = & \frac{1}{\Omega} \sum_{\mathbf{G}_1 \mathbf{G}_2} \rho_{n\mathbf{K}, n'\mathbf{K}'}^*(\mathbf{G}_1) [-W_{\mathbf{G}_1 \mathbf{G}_2}^T(\mathbf{K}' - \mathbf{K}, \Delta\omega = 0)] \\ & \times \rho_{m\mathbf{K}+\mathbf{Q}, m'\mathbf{K}'+\mathbf{Q}}(\mathbf{G}_2), \end{aligned} \quad (24)$$

as shown in Figs. 3(b) and 3(c). Therefore, the calculation of the ladder photon self-energy $\Pi_{\mu\nu}^{\text{ladd}}$ consists of Eqs. (18), (19), and (22), where instead of the photon BSE-Fock kernel Eq. (23), we utilize the ordinary BSE-Fock kernel Eq. (24). The calculation procedure of the ladder photon self-energy is also illustrated by Feynman diagrams in Fig. 4. This computational approach for the RPA + ladder photon self-energy is completely equivalent to solving the Bethe-Salpeter equation within the framework of the widely used time-dependent screened Hartree-Fock (TDSHF) approximation [39–46]. More specifically, this method consists of the following steps: (1) We solve BSE Eq. (19) (i.e., TDSHF-BSE but without the Hartree term), we obtain the ladder four-point polarizability \mathcal{K} , and from it we derive the ladder irreducible polarizability Π^{ladd} (as shown in Fig. 4). (2) We separately derive the RPA irreducible polarizability Π^{RPA} Eq. (16). (3) Finally, we sum two terms in total irreducible polarizability $\Pi = \Pi^{\text{RPA}} + \Pi^{\text{ladd}}$, which then enters in Dyson Eq. (12). So, this procedure neglects the Hartree term in BSE Eq. (19),

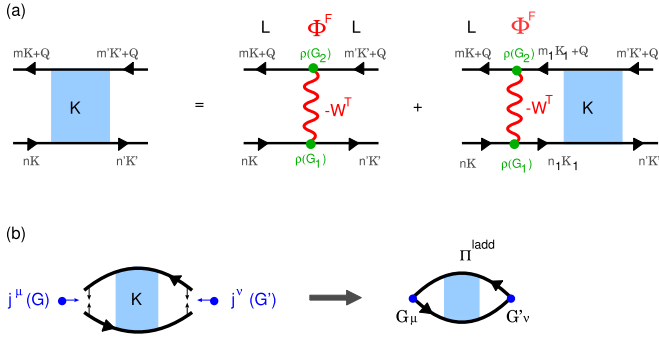


FIG. 4. The calculation procedure for the ladder photon self-energy Π^{ladd} . (a) The matrix equation for the ladder four-point polarizability \mathcal{K} . (b) The ladder photon self-energy Π^{ladd} is obtained when the fermionic lines in \mathcal{K} are contracted, multiplied by corresponding current vertices j^μ and j^ν , and summed over bands and wave vectors, $\Pi^{\text{ladd}} = -\frac{1}{\Omega c} \sum_{nm\mathbf{K}} \sum_{n'm'\mathbf{K}'} j^\mu \mathcal{K}^{\text{ladd}} [j^\nu]^*$.

however, it is finally included in Eq. (12). The advantage of this method is that it allows that (less demanding) Π^{RPA} and (more demanding) Π^{ladd} can be calculated separately, at different levels of accuracy. The RPA time-ordered screened Coulomb interaction W^T , which enters the Fock kernel Eq. (24), is obtained by solving the Dyson equation

$$W_{\mathbf{G}\mathbf{G}'}^T(\mathbf{Q}, \omega) = v_{\mathbf{G}\mathbf{G}'}(\mathbf{Q}) + \sum_{\mathbf{G}_1\mathbf{G}_2} v_{\mathbf{G}\mathbf{G}_1}(\mathbf{Q}) \chi_{\mathbf{G}_1\mathbf{G}_2}^0(\mathbf{Q}, \omega) W_{\mathbf{G}_2\mathbf{G}'}^T(\mathbf{Q}), \quad (25)$$

where the bare Coulomb interaction matrix is

$$v_{\mathbf{G}_1\mathbf{G}_2}(\mathbf{Q}) = \delta_{\mathbf{G}_1\parallel, \mathbf{G}_2\parallel} \frac{2\pi}{L|\mathbf{Q} + \mathbf{G}_1\parallel|} \times \int_{-L/2}^{L/2} dz_1 dz_2 e^{-i\mathbf{G}_{z1}z_1} e^{-i\mathbf{Q} + \mathbf{G}_1\parallel|z_1 - z_2|} e^{i\mathbf{G}_2z_2}. \quad (26)$$

The truncated interaction Eq. (26) excludes the spurious Columob interaction between the phosphorene replicas in the superlattice arrangement and it is crucial to include it in the calculations, namely, the interactions v and W enter the the BSE-Fock kernel Eq. (24), which represents the interaction energy between excited electrons and holes (long-ranged monopole-monopole interaction). If in Eq. (24) one would use bulk v instead of truncated v , given by Eq. (26), this would result in the inclusion of the spurious interaction between excited electrons and holes in different phosphorene supercells, which is not a negligible contribution, due to its long-range character. The RPA irreducible polarizability is defined as

$$\chi_{\mathbf{G}\mathbf{G}'}^0(\mathbf{Q}, \omega) = \frac{1}{\Omega} \sum_{nm\mathbf{K}} \rho_{n\mathbf{K}, m\mathbf{K}+\mathbf{Q}}(\mathbf{G}) \rho_{n'\mathbf{K}, m'\mathbf{K}+\mathbf{Q}}^*(\mathbf{G}') \times \frac{(f_{n\mathbf{K}} - f_{m\mathbf{K}+\mathbf{Q}})}{\hbar\omega + E_{n\mathbf{K}} - E_{m\mathbf{K}+\mathbf{Q}} + i\delta \text{sgn}(E_{m\mathbf{K}+\mathbf{Q}} - E_{n\mathbf{K}})}, \quad (27)$$

where the charge vertices are

$$\rho_{n\mathbf{K}, m\mathbf{K}+\mathbf{Q}}(\mathbf{G}) = \int_{\Omega} d\mathbf{r} \phi_{n\mathbf{K}}^*(\mathbf{r}) e^{-i(\mathbf{Q}+\mathbf{G})\mathbf{r}} \phi_{m\mathbf{K}+\mathbf{Q}}(\mathbf{r}). \quad (28)$$

A. Optical limit $Q \approx 0$

Here we shall explore electromagnetic modes in 2D crystals in the frequency range going from the terahertz (THz) up to ultraviolet (UV) values, i.e., $\hbar\omega \lesssim 4\text{ eV}$. The corresponding wavelength is then much larger than the 2D crystal thickness and the parallel unit cell size, i.e., $\lambda = \frac{2\pi c}{\omega} \gg L, a$. Therefore, the electromagnetic field variations on the scale of one unit cell are irrelevant and the crystal-local-field effects (CLFE) can be freely excluded from consideration. Setting $\mathbf{G} = \mathbf{G}' = 0$ into Dyson's equation yields

$$D_{\mu\nu}(\mathbf{Q}, \omega) = D_{\mu\nu}^0(\mathbf{Q}, \omega) + \sum_{\alpha, \beta=1}^3 D_{\mu\alpha}^0(\mathbf{Q}, \omega) \Pi_{\alpha\beta}(\mathbf{Q}, \omega) D_{\beta\nu}(\mathbf{Q}, \omega). \quad (29)$$

Here we have introduced the term $\Pi_{\mu\nu}(\mathbf{Q}, \omega) = \Pi_{\mu\nu, \mathbf{G}=0\mathbf{G}'=0}(\mathbf{Q}, \omega)$, $D_{\mu\nu}^0(\mathbf{Q}, \omega) = D_{\mu\nu, \mathbf{G}=0\mathbf{G}'=0}^0(\mathbf{Q}, \omega)$. Dyson's equation [see Eq. (29)] is expressed in terms of abstract tensors D and Π , but we shall rewrite it in terms of measurable quantities, i.e., the electric field E_μ and conductivity $\sigma_{\mu\nu}$. The screened vector potential produced by an external current \mathbf{j}^{ext} is defined as

$$A_\mu(\mathbf{Q}, \omega) = \sum_{\nu=1}^3 D_{\mu\nu}(\mathbf{Q}, \omega) j_\nu^{\text{ext}}(\mathbf{Q}, \omega), \quad (30)$$

while the bare vector potential is analogously defined as $\mathbf{A}^{\text{ext}} = \hat{D}^0 \mathbf{j}^{\text{ext}}$. In the $\Phi = 0$ gauge, the connection between the vector potential and the electric field is

$$E_\mu(\mathbf{Q}, \omega) = \frac{i\omega}{c} A_\mu(\mathbf{Q}, \omega). \quad (31)$$

Moreover, combining formulas $\mathbf{j}^{\text{ind}} = \hat{\Pi} \mathbf{A}$, $\mathbf{j}^{\text{ind}} = \hat{\sigma} \mathbf{E}$, and Eq. (31), one obtains the connection between the photon self-energy and the conductivity tensor:

$$\sigma_{\mu\nu}(\omega) = \frac{c}{i\omega} \Pi_{\mu\nu}(\mathbf{Q}, \omega). \quad (32)$$

After substitution of Eqs. (30)–(32) into Eq. (29), we obtain the Dyson equation for the screened electric field,

$$E_\mu(\mathbf{Q}, \omega) = E_\mu^{\text{ext}}(\mathbf{Q}, \omega) + \sum_{\alpha, \beta=1}^3 \Gamma_{\mu\alpha}(\mathbf{Q}, \omega) \sigma_{\alpha\beta}(\mathbf{Q}, \omega) E_\beta(\mathbf{Q}, \omega), \quad (33)$$

where we introduce the propagator of the free electric field:

$$\Gamma_{\mu\nu}(\mathbf{Q}, \omega) = \frac{i\omega}{c} D_{\mu\nu}^0(\mathbf{Q}, \omega). \quad (34)$$

The formal solution of Eq. (33) is therefore

$$\mathbf{E}(\mathbf{Q}, \omega) = \hat{\epsilon}^{-1}(\mathbf{Q}, \omega) \mathbf{E}^{\text{ext}}(\mathbf{Q}, \omega), \quad (35)$$

where the dielectric tensor is defined as

$$\epsilon_{\mu\nu}(\mathbf{Q}, \omega) = \delta_{\mu\nu} - \sum_{\alpha=1}^3 \Gamma_{\mu\alpha}(\mathbf{Q}, \omega) \sigma_{\alpha\nu}(\mathbf{Q}, \omega). \quad (36)$$

In the THz and UV regions ($\omega \lesssim 4\text{ eV}$) and for the parallel wave vector $QL \ll 1$, the complex perpendicular wave vector

goes as $\beta L \rightarrow 0$. Using Eq. (34) and expressions defined in Eqs. (13) and (14), the free electric field propagator can be approximated as

$$\begin{aligned} \Gamma(\mathbf{Q}, \omega) = & -\frac{2\pi\beta L}{\omega} \mathbf{Q}_0 \cdot \mathbf{Q}_0 - \frac{2\pi\omega L}{\beta c^2} \mathbf{e}_s \cdot \mathbf{e}_s \\ & - \left[\frac{4i\pi}{\omega} + \frac{2\pi Q^2 L}{\beta\omega} \right] \mathbf{z} \cdot \mathbf{z}. \end{aligned} \quad (37)$$

In the optical limit, the conductivity tensor can be approximated as a diagonal matrix,

$$\sigma_{\mu\nu}(\mathbf{Q} \approx 0, \omega) \approx \sigma_{\mu}(\omega) \delta_{\mu\nu}, \quad (38)$$

where, following Eq. (32), the optical conductivity is given by

$$\sigma_{\mu}(\omega) = \frac{c}{i\omega} \Pi_{\mu\mu, \mathbf{G}=0\mathbf{G}'=0}(\mathbf{Q}=0, \omega). \quad (39)$$

According to Eq. (15), the optical conductivity can also be separated into the RPA and ladder contributions. Moreover, because here we study doped semiconductors, it is useful to additionally separate the RPA term into intra- and interband contributions such that total conductivity can be written as

$$\sigma_{\mu}(\omega) = \sigma_{\mu}^{\text{intra}}(\omega) + \sigma_{\mu}^{\text{inter}}(\omega) + \sigma_{\mu}^{\text{ladd}}(\omega). \quad (40)$$

After using Eqs. (39) and (16), the intraband ($n = m$) RPA optical conductivity is defined as

$$\sigma_{\mu}^{\text{intra}}(\omega) = i \frac{e^2}{m} \frac{n_{\mu}}{\omega + i\eta_{\text{intra}}}, \quad (41)$$

where the effective number of charge carriers is

$$n_{\mu} = -\frac{m}{\Omega e^2} \sum_n \sum_{\mathbf{K} \in 1.\text{SBZ}} \frac{\partial f_{n\mathbf{K}}}{\partial E_{n\mathbf{K}}} |j_{n\mathbf{K}, n\mathbf{K}}^{\mu}(\mathbf{G}=0)|^2. \quad (42)$$

The interband ($n \neq m$) RPA optical conductivity is given by

$$\begin{aligned} \sigma_{\mu}^{\text{inter}}(\omega) = & -i \frac{\hbar}{\Omega} \sum_{n \neq m} \sum_{\mathbf{K} \in 1.\text{SBZ}} \frac{f_{n\mathbf{K}} - f_{m\mathbf{K}}}{E_{n\mathbf{K}} - E_{m\mathbf{K}}} \\ & \times \frac{|j_{n\mathbf{K}, m\mathbf{K}}^{\mu}(\mathbf{G}=0)|^2}{\hbar\omega + E_{n\mathbf{K}} - E_{m\mathbf{K}} + i\eta_{\text{inter}}}. \end{aligned} \quad (43)$$

Following the definition given in Eq. (39), the ladder optical conductivity is explicitly given by

$$\sigma_{\mu}^{\text{ladd}}(\omega) = \frac{c}{i\omega} \Pi_{\mu\mu, \mathbf{G}=0\mathbf{G}'=0}^{\text{ladd}}(\mathbf{Q}=0, \omega), \quad (44)$$

where the calculation of the ladder self-energy is described by Eqs. (18)–(28). We stated previously that neglecting the CLFE in the photon self-energy Π is fully justified. However, while calculating the ladder contribution Π^{ladd} , one should be careful when neglecting CLFE in the Fock kernel [see Eq. (24)]. Short range $\mathbf{K}' - \mathbf{K} \sim 2\pi/a, 2\pi/L$ electron-electron (or hole-hole) scattering processes can occur, thereby making exclusion of CLFE in the Coulomb interaction $W^T(\mathbf{K}' - \mathbf{K})$ not completely justified. Nevertheless, as we shall demonstrate in Sec. III, since the main contribution to the exciton binding energy comes from the scattering processes with $\mathbf{K}' - \mathbf{K} < 2\pi/a, 2\pi/L$, disregarding the CLFE in the Fock-kernel Eq. (24) still serves as a satisfactory approximation. In this approximation, Dyson's Eq. (25) becomes a scalar

equation, where the solution is

$$W^T(\mathbf{Q}, \omega) = v_Q / \epsilon(\mathbf{Q}, \omega), \quad (45)$$

with the longitudinal dielectric function given by

$$\epsilon(\mathbf{Q}, \omega) = 1 - v_Q \chi^0(\mathbf{Q}, \omega). \quad (46)$$

Using Eq. (26), the bare Coulomb interaction is

$$v_Q = v_{\mathbf{G}=0\mathbf{G}'=0}(\mathbf{Q}) = \frac{4\pi}{Q^2} \frac{QL + e^{-QL} - 1}{QL}, \quad (47)$$

and by following Eq. (27) the RPA irreducible polarizability becomes

$$\begin{aligned} \chi^0(\mathbf{Q}, \omega) = & \chi_{\mathbf{G}=0\mathbf{G}'=0}^0(\mathbf{Q}, \omega) = \frac{1}{\Omega} \sum_{m\mathbf{K}} (f_{n\mathbf{K}} - f_{m\mathbf{K}+\mathbf{Q}}) \\ & \times \frac{|\rho_{n\mathbf{K}, m\mathbf{K}+\mathbf{Q}}(\mathbf{G}=0)|^2}{\hbar\omega + E_{n\mathbf{K}} - E_{m\mathbf{K}+\mathbf{Q}} + i\delta \text{sgn}(E_{m\mathbf{K}+\mathbf{Q}} - E_{n\mathbf{K}})}. \end{aligned} \quad (48)$$

1. Spectra of electromagnetic modes

In anisotropic 2D crystals (such as phosphorene), the intensity of the electromagnetic modes depends on the direction of its propagation \mathbf{Q}_0 , such that \mathbf{Q}_0 cannot be chosen arbitrarily and the electric field propagator matrix in Eq. (37) remains generally nondiagonal. However, here we shall restrict our consideration to the electromagnetic modes which propagate in $\mathbf{Q}_0 = \mathbf{x}$ and $\mathbf{Q}_0 = \mathbf{y}$ directions, i.e., along the phosphorene \mathbf{a}_1 and \mathbf{a}_2 crystal axes, respectively. For example, if the electromagnetic mode propagates in the $\mathbf{Q}_0 = \mathbf{x}$ direction, the free electric field propagator in Eq. (37) becomes the diagonal matrix

$$\Gamma_{\mu\nu}(Q\mathbf{x}, \omega) = \Gamma_{\mu} \delta_{\mu\nu}, \quad (49)$$

where $\Gamma_x = -\frac{2\pi\beta L}{\omega}$, $\Gamma_y = -\frac{2\pi\omega L}{\beta c^2}$, and $\Gamma_z = -\frac{4i\pi}{\omega} - \frac{2\pi Q^2 L}{\beta\omega}$. After combining Eqs. (36), (38), and (49), the dielectric tensor can be expressed explicitly as

$$\epsilon_{\mu\mu}(Q\mathbf{x}, \omega) = 1 - \Gamma_{\mu} \sigma_{\mu}(\omega). \quad (50)$$

The electromagnetic mode propagation in the $\mathbf{Q}_0 = \mathbf{y}$ direction is given by making the substitution $\Gamma_x \leftrightarrow \Gamma_y$. Finally, by following Eq. (35), the screened electric field is

$$E_{\mu}(\mathbf{Q}, \omega) = E_{\mu}^{\text{ext}}(\mathbf{Q}, \omega) / \epsilon_{\mu\mu}(\mathbf{Q}, \omega). \quad (51)$$

The induced current is defined as a response function of the screened field via

$$j_{\mu}^{\text{ind}}(\mathbf{Q}, \omega) = \sigma_{\mu}(\omega) E_{\mu}(\mathbf{Q}, \omega). \quad (52)$$

Substitution of Eq. (51) into the above equation yields the induced current as a response to the external field as

$$j_{\mu}^{\text{ind}}(\mathbf{Q}, \omega) = \sigma_{\mu}^{\text{scr}}(\mathbf{Q}, \omega) E_{\mu}^{\text{ext}}(\mathbf{Q}, \omega), \quad (53)$$

where we introduce the screened conductivity:

$$\sigma_{\mu}^{\text{scr}}(\mathbf{Q}, \omega) = \sigma_{\mu}(\omega) / \epsilon_{\mu\mu}(\mathbf{Q}, \omega). \quad (54)$$

The real part of the optical conductivity $\text{Re}[\sigma_{\mu}(\omega)]$ gives us information about the intensity of optically active interband transitions and excitons in the system. On the other hand, the real part of the screened conductivity $\text{Re}[\sigma_{\mu}^{\text{scr}}(\mathbf{Q}, \omega)]$ gives information about the collective electronic modes and

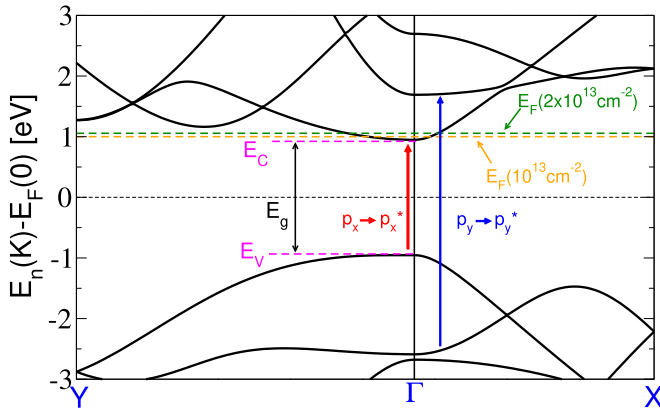


FIG. 5. The phosphorene band structure. Yellow and green dashed lines denote the Fermi energy in doped phosphorene at $T = 284$ K when $n = 10^{13} \text{ cm}^{-2}$ and $n = 2 \times 10^{13} \text{ cm}^{-2}$, respectively. The pristine Fermi energy is set to zero. The Fermi energies which correspond to doped phosphorene with $n = 10^{13} \text{ cm}^{-2}$ and $n = 2 \times 10^{13} \text{ cm}^{-2}$ are $E_F - E_C = 52 \text{ meV}$ and 108 meV , respectively.

hybridizations between electronic modes and photons, such as plasmon-polaritons and exciton-polaritons. Therefore, the present formulation enables us to explore a wide class of electromagnetic modes, such as evanescent $\omega < Qc$, radiative $\omega > Qc$, transverse s(TE) $\sigma_{x(y)}^{\text{scr}}[Q\mathbf{y}(\mathbf{x}), \omega]$, or longitudinal p(TM) $\sigma_{x(y)}^{\text{scr}}[Q\mathbf{x}(\mathbf{y}), \omega]$ single particle and collective electromagnetic modes.

2. Clarification of terminology

To facilitate the understanding of the text, we shall first clarify some of the labels and definitions that are often used below. The screened Coulomb interaction in pristine phosphorene obtained from the KS wave function and energies Eqs. (45)–(48) will be denoted as W_0^0 . The same screened interaction but in doped phosphorene will be denoted as W_0^{dop} . Similarly, Green's functions Eq. (21) constructed from the pristine or doped phosphorene KS wave function and energies will be denoted as G_0^0 or G_0^{dop} , respectively. In pristine semiconductors, the energetic onset for the creation of non-interacting (RPA) electron-hole pairs is the band-gap energy $E_g = E_C - E_V$, where E_V is the top of the valence band and E_C is the bottom of the conductive band, also denoted in the phosphorene band structure shown in Fig. 5. In semiconductors doped by electrons ($n > 0$), and for reasonably small temperatures ($T < 300$ K), the value E_g should be, due to Pauli blocking, corrected by an amount $2(E_F - E_C)$ such that the onset for the RPA electron-hole pair creation becomes $E_g + 2(E_F - E_C)$. Consequently, the exciton binding energy is defined as

$$\Delta = E_g + 2\alpha(E_F - E_C) - \hbar\omega_{\text{ex}}, \quad (55)$$

where $\alpha = 0$ and 1 for pristine ($n = 0$) and doped ($n > 0$) semiconductors, respectively, and $\hbar\omega_{\text{ex}}$ is the exciton energy. The abbreviation RPA(G_0^i), where $i = 0$ or dop, will denote the RPA method in which the Green's functions G_0^i is inserted. Also, with BSE(G_0^i, W_0^i) ($i = 0$, dop) we denote the RPA + ladder method, where the Green's functions G_0^i are used, and the screened Coulomb interaction W_0^i enters the BSE-

Fock kernel Eq. (24). In all cases, it is understood that the Green's function G_0^i is constructed from GW_0 energies $E_{n\mathbf{K}}^i$ ($i = 0$, dop). The extra screening that comes from the doping is labeled as $\Delta W = W_0^{\text{dop}} - W_0^0$.

B. Computational details

In the first stage of calculations, we determine the phosphorene KS wave functions $\phi_{n\mathbf{K}}$ and energies $E_{n\mathbf{K}}$ using a plane-wave self-consistent field DFT code (PWSCF) within the QUANTUM ESPRESSO (QE) package [56]. The core-electron interactions were approximated by norm-conserving pseudopotentials [57] and the exchange-correlation potential by the Perdew-Burke-Ernzerhof generalized gradient approximation [58]. To calculate the ground-state electronic density we, have used a $26 \times 37 \times 1$ Monkhorst-Pack K-point mesh [59] of the first Brillouin zone and for the plane-wave cut-off energy, we have chosen 50 Ry. We have used the orthorhombic Bravais lattice where the unit cell lattice constants of $a = 4.631 \text{ \AA}$ and $b = 3.3062 \text{ \AA}$, while the separation between phosphorene layers is given by $L = 17.11 \text{ \AA}$. The doped phosphorene was simulated such that extra electrons were injected ($n > 0$) or extracted ($n < 0$) from the unit cell and the compensating jellium background was inserted to neutralize the unit cell. The electronic and atomic relaxation were provided for each doping concentration n until a maximum force below 0.001 Ry/a.u. was obtained. The RPA optical conductivity Eqs. (41)–(43) and screened Coulomb interaction in Eqs. (45)–(48) were calculated by using a $109 \times 151 \times 1$ K-point mesh, and the band summations were performed over 50 bands. The dimension of $\{\mathbf{K}, n\}$ -space used in the calculation of the BSE-Fock kernel Eq. (24), the four-point polarizability matrix Eq. (19), the ladder photon self-energy Eq. (18), and the ladder optical conductivity Eq. (44) consists of $53 \times 75 \times 1$ Monkhorst-Pack K-points and two (one valence and one conduction) bands. The CLFE are not included in the calculation. The DFT calculations underestimate the semiconducting band gap which then influences the total excitation spectra as well as the exciton energy $\hbar\omega_{\text{ex}}$. To overcome this issue, the energies $E_{n\mathbf{K}}$ used to calculate the RPA + ladder conductivities (for each doping concentration n) were obtained by means of the GW quasiparticle approximation as implemented within the real space projector augmented wave function code GPAW [60,61]. The corresponding ground state parameters and crystal structures follow those outlined for the QE calculations. We have used the $20 \times 30 \times 1$ K-grid. 100 bands for the GW calculation were used, and the energy cutoff for the local field effect vectors is 80 eV . The self-consistent GW_0 method with $n = 3$ steps was used, where energies in the Green's functions are iterated.

To check the accuracy of the here-introduced RPA + ladder approximation, the results for exciton spectra, exciton energies $\hbar\omega$, and binding energies Δ are compared with results obtained by means of GPAW, where optical properties with excitonic effects included can be obtained by solving the BSE effective two-particle Hamiltonian. To solve the BSE within the GPAW code, we have used the $53 \times 75 \times 1$ K-grid, 10 eV energy cutoff for the CLFE, and four (two valence and two conduction) bands. The broadening parameter was set to 0.05 eV .

III. RESULTS

Here we shall first present the results for the optical conductivity $\text{Re } \sigma_x(\omega)$ in doped phosphorene for various doping concentrations n , as y polarized light yields no excitonic response [36]. Then we shall present the results for the screened conductivity $\text{Re } \sigma_x^{\text{scr}}(\mathbf{Q}, \omega)$ for different wave vector directions, i.e., Q_y and Q_x , where transverse exciton-polaritons and longitudinal excitons are found, respectively. Finally, we shall present results for $\text{Re } \sigma_{x(y)}^{\text{scr}}(Q_{x(y)}, \omega)$ in the THz frequency region, where longitudinal plasmon-polaritons are formed.

A. Optical conductivity in doped phosphorene

Figure 6(a) shows plots for the RPA(G_0^0) (black) and BSE(G_0^0, W_0^0) (magenta) optical conductivities in pristine phosphorene. The GW band gap in pristine phosphorene is $E_g = 2.05$ eV, and the RPA conductivity shows an onset for electron-hole creation at the same energy. The BSE(G_0^0, W_0^0)

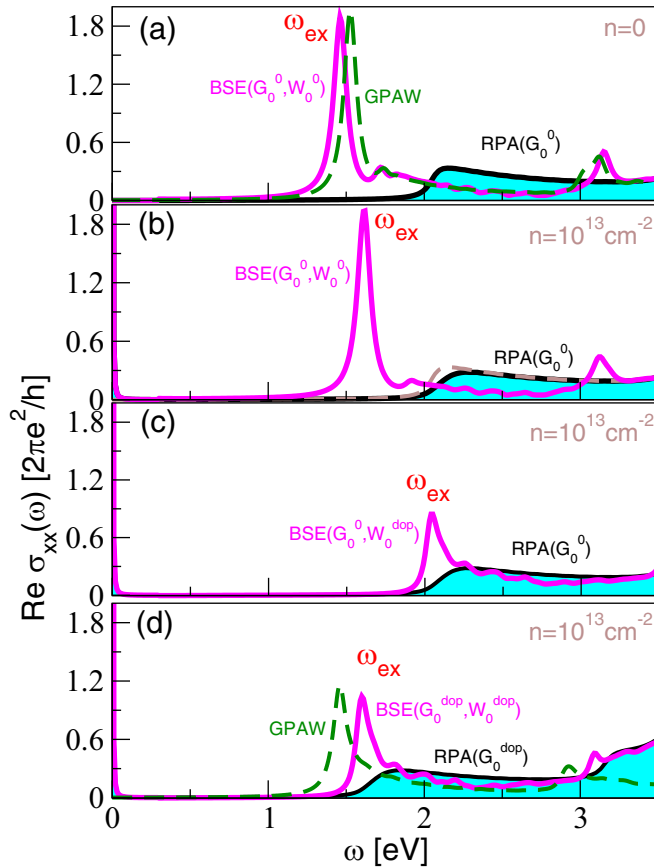


FIG. 6. The RPA (black) and the RPA + ladder (magenta) optical conductivities in (a) pristine and (b)–(d) doped phosphorene. (b) G_0^0 and W_0^0 are used at both the RPA and ‘RPA + ladder’ level of calculations. (c) G_0^0 is used at RPA and G_0^0 and W_0^{dop} are used at the RPA + ladder level. (d) G_0^{dop} and W_0^{dop} are used, at both RPA and RPA + ladder level of calculations. The brown dashed line in (b) shows the RPA conductivity in pristine phosphorene for comparison. In (b) and (c), the occupation factors $f_{n\mathbf{K}}$ appearing in the Green’s function G_0^0 are taken to be as in a doped crystal. Green dashed lines in (a) and (d) depict the result obtained by solving GW-BSE using the GPAW package.

conductivity shows a strong exciton at $\hbar\omega_{\text{ex}} = 1.45$ eV whose binding energy, according to Eq. (55), is $\Delta = 600$ meV. This value underestimates the theoretical results $\Delta \sim 0.6 - 0.8$ eV reported in Refs. [28–33] as well as experimental results $\Delta \sim 0.9$ eV reported in Refs. [35,36,38]. However, the exciton binding energy is not easy to determine experimentally because (1) the band gap E_g is difficult to measure accurately, (2) even very small substrate-induced doping of the phosphorene conducting/valence bands causes a screening shift ΔW which can significantly change the exciton binding energy, and (3) the substrate Coulomb screening also influences the exciton binding energy. All these may lead to the disparate results seen, such that, for example, in Ref. [36] the binding energy is estimated to be $\Delta = 0.9$ eV, and in Refs. [33,37], where the phosphorene is deposited on the SiO_2/Si substrate, it is estimated as $\Delta = 0.3$ eV. Still, to ensure that the results obtained using the RPA + ladder approach are satisfactorily accurate, the green dashed line in Fig. 6(a) shows the result obtained by solving GW-BSE using the GPAW package. Besides very good qualitative agreement between the two spectra, the GPAW exciton energy is $\hbar\omega_{\text{ex}} = 1.51$ eV and the exciton binding energy is $\Delta = 540$ meV, both of which are in satisfactorily good agreement with the results of our calculations. Also, while it is often assumed that the exciton energy $\hbar\omega$ does not depend on the substrate screening [7], this is not always the case. Below, we shall decompose different mechanisms affecting the final exciton spectra when the phosphorene is doped by electrons.

Figure 6(b) shows the RPA(G_0^0) and BSE(G_0^0, W_0^0) optical conductivities in doped phosphorene, where $n = 10^{13} \text{ cm}^{-2}$. Here the pristine Green’s function G_0^0 and the screened interaction W_0^0 are used at both the RPA and RPA + ladder level of calculation. However, since the goal is to explore what the impact of the Pauli blocking on the exciton spectral weight and the binding energy, the occupation factors $f_{n\mathbf{K}}$ which appear in the Green’s functions G_0^0 are taken to be as in the doped sample. The same applies for the results presented in Fig. 6(c). Thus, the only effect of the doping here is the extra population of the phosphorene conduction band E_C , which at $T = 284$ K shifts the Fermi energy by only 52 meV above E_C , as can be seen in Fig. 5. The Pauli blocking reduces the phase space for direct interband electron-hole excitations and consequently blueshifts and reduces the intensity of the RPA absorption onset, which can be clearly seen when the black line is compared with the brown-dashed line showing the pristine RPA(G_0^0) conductivity. Consequently, the comparison between BSE(G_0^0, W_0^0) conductivities in Figs. 6(a) and 6(b) demonstrates how Pauli blocking affects the exciton energy. It can be noticed that the exciton is blueshifted to $\hbar\omega_{\text{ex}} = 1.61$ eV such that its binding energy becomes $\Delta = 544$ meV. We can therefore conclude that the lack of phase space due to Pauli blocking reduces the exciton binding energy by 56 meV without affecting its oscillatory strength. Figure 6(c) shows the RPA(G_0^0) and BSE(G_0^0, W_0^{dop}) optical conductivities. Here at the BSE stage of calculation, i.e., in the Fock kernel Eq. (24), the doped screened interaction W_0^{dop} is used. It can be noticed that an additional screening $\Delta W_0 = W_0^{\text{dop}} - W_0^0$ significantly reduces the exciton binding energy and the oscillatory strength. More precisely, the exciton binding energy is reduced to $\Delta = 114$ meV. Interestingly, even such a small doping significantly changes the

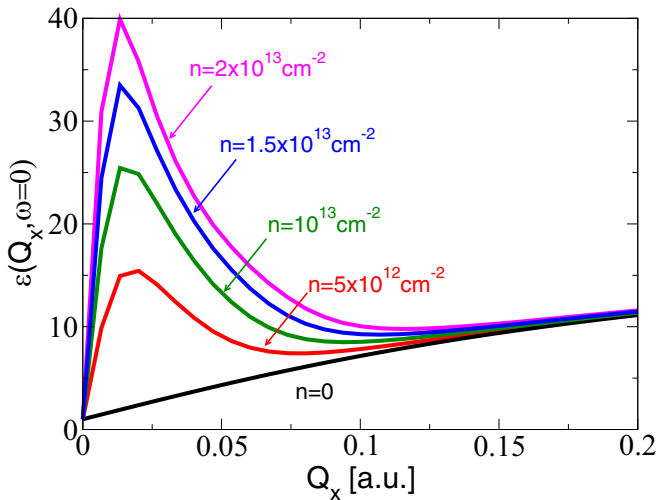


FIG. 7. The static dielectric function $\epsilon(Q_x, \omega = 0)$ in doped phosphorene for different doping concentrations, i.e., $n = 0$ (black), $n = 5 \times 10^{12} \text{ cm}^{-2}$ (red), $n = 10^{13} \text{ cm}^{-2}$ (green), $n = 1.5 \times 10^{13} \text{ cm}^{-2}$ (blue) and $n = 2 \times 10^{13} \text{ cm}^{-2}$ (magenta).

exciton identity, as even a small injection of charge carriers into the conduction band results in strong metallic screening that radically reduces the static interaction $W(Q, \omega = 0) = v_Q/\epsilon(Q, \omega = 0)$, and thus the exciton binding energy and intensity. Figure 7 shows the comparison between the static dielectric function $\epsilon(Q_x, \omega = 0)$ in pristine phosphorene (black) and in the various cases of doped phosphorene (red, green, blue, and magenta). While in the pristine phosphorene the dielectric function shows standard linear behavior $\epsilon(Q_x, \omega = 0) = 1 + \alpha_x Q_x$, where $\alpha_x = 68$, in the doped phosphorene it strongly overestimates the pristine value, especially in the long wave-length limit $Q \approx 0$. The same is valid for the Q_y direction, where $\alpha_y = 58$. Considering that $W(Q \approx 0)$ is exactly responsible for the formation of the electron-hole bound state, it is not surprising that the exciton is significantly degraded. Finally, Fig. 6(d) shows the RPA(G_0^{dop}) and the BSE($G_0^{\text{dop}}, W_0^{\text{dop}}$) optical conductivities where the total screened interaction W_0^{dop} , is used at both the RPA and RPA + ladder levels of calculations. Strong metallic screening ΔW^0 reduces the band gap to $E_g = 1.58 \text{ eV}$, which also influences the exciton energy $\hbar\omega_{\text{ex}} = 1.6 \text{ eV}$, as well as the exciton binding energy $\Delta = 84 \text{ meV}$. We emphasize here that the final drop in the exciton binding energy Δ of 516 meV and the drop of the effective band gap $E_g + 2\alpha(E_F - E_C)$ of 366 meV do not cancel, which results in a 150 meV blueshift of the exciton energy $\hbar\omega_{\text{ex}}$. Green dashed line in Fig. 6(d) shows the optical conductivity obtained by using the GPAW package. The qualitative agreement with the RPA + ladder spectrum is still satisfactory good, however, the GPAW exciton at $\hbar\omega = 1.47 \text{ eV}$ is 130 meV redshifted in comparison with the RPA + ladder exciton providing its larger binding energy of $\Delta = 214 \text{ meV}$. This disagreement is probably because the screened Coulomb interaction, which is very sensitive on small doping (see Fig. 7), is calculated more accurately within the RPA + ladder method than using the GPAW method. In fact, in our method we use a denser k-point mesh at the RPA stage of calculations

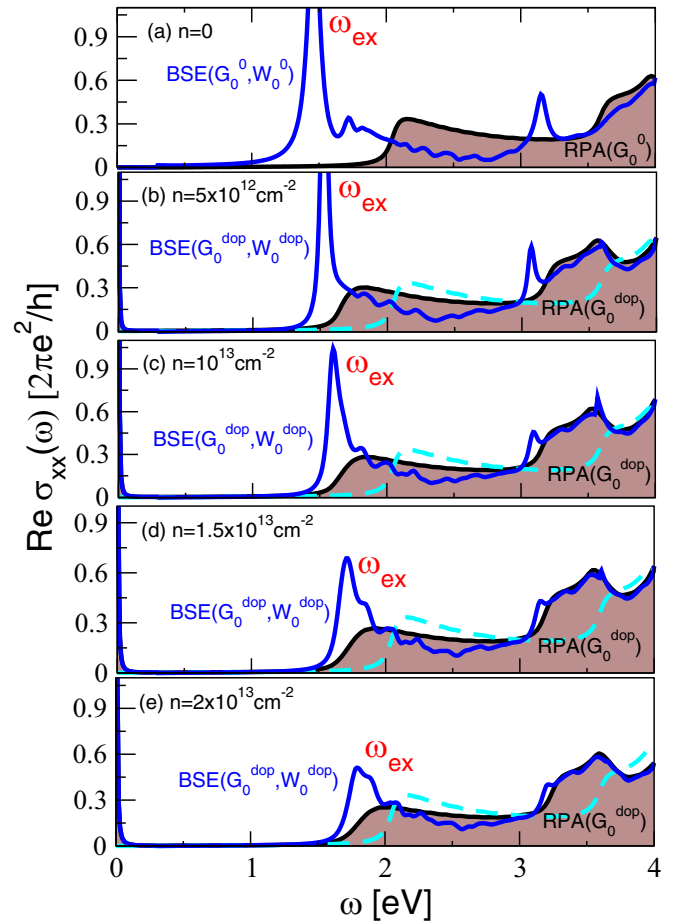


FIG. 8. Evolution of phosphorene exciton as a function of excess electron concentrations (a) $n = 0$, (b) $n = 5 \times 10^{12} \text{ cm}^{-2}$, (c) $n = 10^{13} \text{ cm}^{-2}$, (d) $n = 1.5 \times 10^{13} \text{ cm}^{-2}$, and (e) $n = 2 \times 10^{13} \text{ cm}^{-2}$. The RPA(G_0^i) ($i = 0, \text{dop}$) optical conductivities are shown with black and BSE(G_0^i, W_0^i) ($i = 0, \text{dop}$) optical conductivities by blue lines. For comparison, cyan dashed lines in (b)–(e) show the pristine RPA(G_0^0) optical conductivity.

(i.e., $109 \times 151 \times 1$), which is allowed by the separability of the method. On the other hand, in the GPAW, both screening and the BSE are done on the same k grid (i.e., $53 \times 75 \times 1$). Also, the Drude and interband contributions to Π^{RPA} are in the RPA + ladder method calculated at different degrees of accuracy compared to the GPAW method. For instance, the GPAW does not include the Drude term. However, the GPAW result still shows a small exciton blueshift of 20 meV in comparison with the undoped case. The similar qualitative behavior, exciton quenching, and blueshift are experimentally and theoretically obtained for the case of doped single-layer TMDs [1,62], which suggests that our method can be used as an accurate tool for simulating the exciton properties as a function of doping.

Figures 8(a)–8(e) show the evolution of the phosphorene exciton as a function of excess electron concentration ($n > 0$). The RPA(G_0^i) ($i = 0, \text{dop}$) optical conductivities are shown with the black lines and the BSE(G_0^i, W_0^i) ($i = 0, \text{dop}$) conductivities with the blue lines. For comparison, in Fig. 8(a) we show the optical conductivities in pristine phosphorene

TABLE I. Phosphorene band gap (E_g), exciton energy ($\hbar\omega_{\text{ex}}$), Fermi energy relative to conduction band ($E_F - E_C$), and exciton binding energy (Δ), according to Eq. (55), for different doping concentrations n .

n [cm $^{-2}$]	E_g [eV]	$\hbar\omega_{\text{ex}}$ [eV]	$E_F - E_C$ [meV]	Δ [meV]
0	2.05	1.45	/	600
0.5×10^{13}	1.62	1.53	19	128
1.0×10^{13}	1.58	1.6	52	84
1.5×10^{13}	1.62	1.71	81	72
2.0×10^{13}	1.64	1.79	108	66

($n = 0$), calculated from G_0^0 and W_0^0 . In Figs. 8(b)–8(e), the optical conductivities for doped samples with $n = 5 \times 10^{12}$ cm $^{-2}$, $n = 10^{13}$ cm $^{-2}$, $n = 1.5 \times 10^{13}$ cm $^{-2}$, and $n = 2 \times 10^{13}$ cm $^{-2}$, respectively, calculated from corresponding G_0^{dop} and W_0^{dop} are presented, while the cyan dashed line shows the RPA(G_0^0) conductivity. It can be clearly seen how excess electron concentration reduces the exciton binding energy and its oscillatory strength in addition to blueshifting the exciton energy $\hbar\omega_{\text{ex}}$. Quantitative values for the band gap E_g , exciton energy $\hbar\omega_{\text{ex}}$, and exciton binding energy Δ (corresponding to Fig. 8) are summarized in Table I. It is clear that an already tiny electron doping of $n = 5 \times 10^{12}$ cm $^{-2}$ causes a drastic drop in the exciton binding energy, i.e., from $\Delta = 600$ meV to 128 meV. Further increase in the electron doping causes a weak additional decrease of the exciton binding energy. What is clearly noticeable from Table I is that excess electrons cause a considerable blueshift of the exciton energy $\hbar\omega_{\text{ex}}$ such that, for example, already moderate electron doping of $n = 2 \times 10^{13}$ cm $^{-2}$ causes a blueshift of about 340 meV. This suggests that increasing doping causes a larger decrease in the exciton binding energy than does a decrease in the effective band gap $E_g + 2(E_F - E_C)$. In Figs. 8(b)–8(e), the increasing intraband (or Drude) contribution to optical conductivity can

be noticed in the THz ($\omega \approx 0$) region. The Drude contribution will be explained in more detail in Sec. III C.

B. Exciton-polaritons

In this section, we explore the strength of hybridization between the phosphorene exciton and free-photons.

Figures 9(a) and 9(b) show the real part of the screened conductivity Eq. (54) in pristine phosphorene as a function of the transfer wave vector \mathbf{Q} along the $\mathbf{Q} = Q_y \mathbf{y}$ and $\mathbf{Q} = Q_x \mathbf{x}$ directions, respectively. The green dotted line represents the light-line $\omega = Qc$, i.e., the dispersion relation of free-photons. Therefore, Figs. 9(a) and 9(b) actually show the intensities of transverse s(TE) and longitudinal p(TM) electromagnetic modes in pristine phosphorene, respectively. The intense pattern in Fig. 9(a) in the evanescent region $\omega < Qc$ represents the intensity of the evanescent transversal exciton ω_{ex}^T that hybridizes weakly with the free photons as it approaches the light line Qc . It can be noticed that the exciton intensity is enhanced and slightly curved toward the light line Qc , indicating a certain hybridization with light and therefore the formation of the exciton-polariton mode $\omega_{\text{ex-pol}}$. The intense signal which continues in the radiative region $\omega > Qc$ represents the radiative transverse exciton ω_{ex}^T , the standard exciton seen in absorption spectra or in photoluminescence spectroscopy. It is of note that the radiative transverse exciton is of somewhat lower intensity than the evanescent transverse exciton. Figure 9(b) shows that the longitudinal exciton ω_{ex}^L , as expected, does not interact with the transverse photons. In Fig. 9(b), it is also obvious that the exciton dispersivity is negligible. This is because in the $Q \rightarrow 0$ limit the dielectric tensor Eq. (50) becomes

$$\epsilon_{xx}(\mathbf{Q}\mathbf{x}, \omega) = 1 + \frac{2\pi L}{c} \sigma_x(\omega),$$

which is very close to one (in nonretarded limit $c \rightarrow \infty$ it is exactly one, as demonstrated in Fig. 7) and the electrical field Eq. (51) and conductivity Eq. (54) are unscreened. Also,

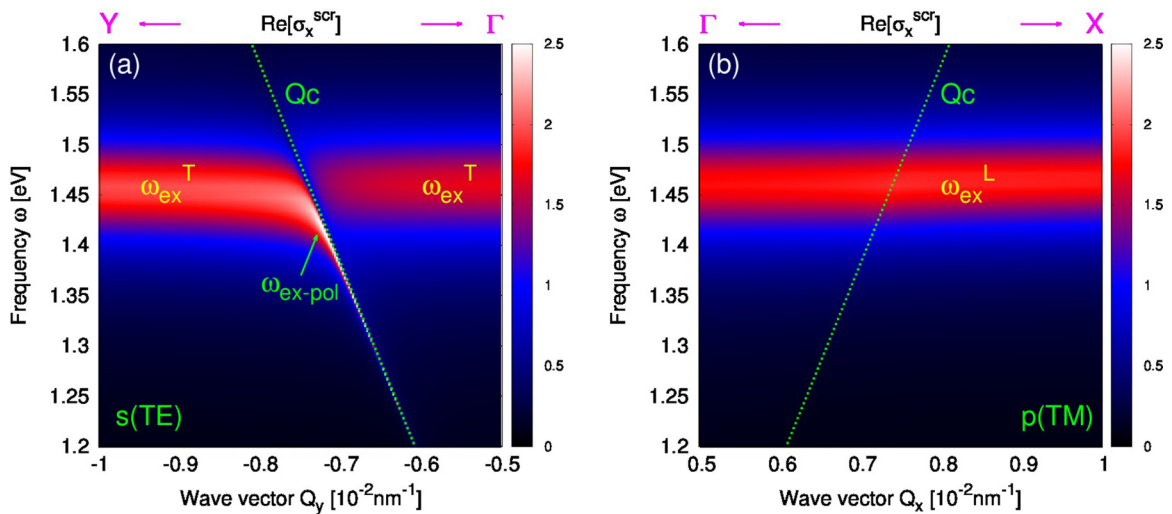


FIG. 9. Real part of the screened conductivity ($\text{Re}[\sigma_{xx}^{\text{scr}}]$) in pristine phosphorene as a function of the transfer wave vector \mathbf{Q} along (a) $\mathbf{Q} = Q_y \mathbf{y}$ and (b) $\mathbf{Q} = Q_x \mathbf{x}$ directions. Weak hybridization between the transverse exciton ω_{ex}^T and the photon Qc forming exciton-polariton $\omega_{\text{ex-pol}}$ can be seen in (a).

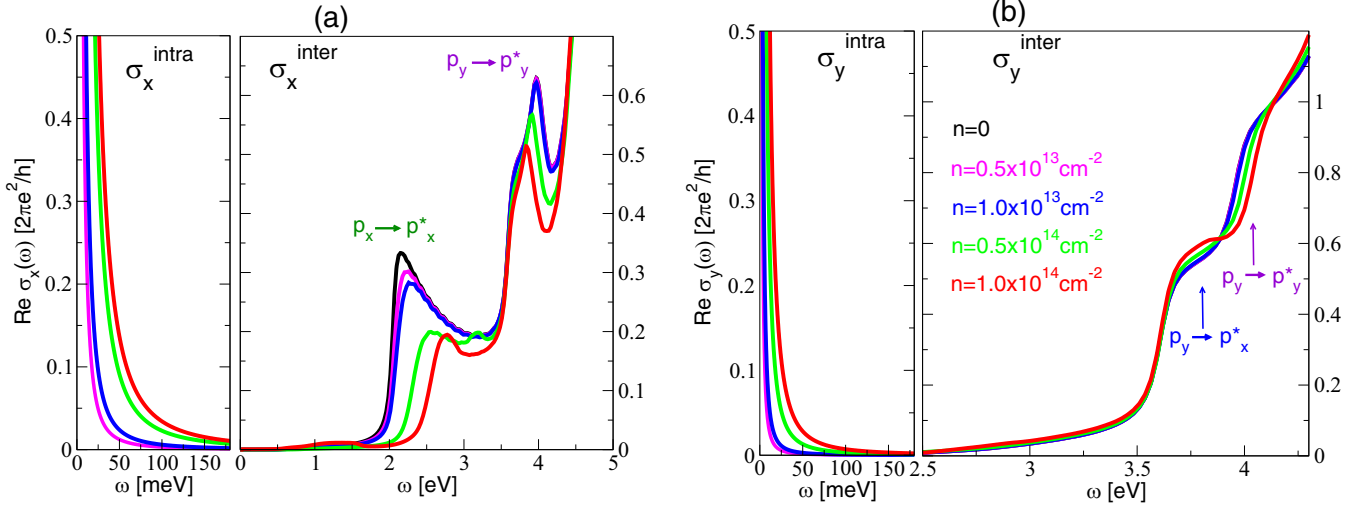


FIG. 10. RPA($G_0^{0,\text{dop}}$) optical conductivities (a) $\sigma_{xx}(\omega)$ and (b) $\sigma_{yy}(\omega)$ in doped phosphorene for various electron concentrations: $n = 0$ (black), $n = 5 \times 10^{12} \text{ cm}^{-2}$ (magenta), $n = 10^{13} \text{ cm}^{-2}$ (blue), $n = 5 \times 10^{13} \text{ cm}^{-2}$ (green), $n = 10^{14} \text{ cm}^{-2}$ (red). Note the panels showing the separate intraband $\sigma_{\mu}^{\text{intra}}$ and interband $\sigma_{\mu}^{\text{inter}}$ contributions.

by consulting Eq. (54), this means that for $Q = 0$ the only contribution to formation of the exciton-polariton state comes from the processes within the unscreened σ (i.e., the ladder term in σ), which means that this state is pure exciton state. For larger Q , the propagator Eq. (49) becomes dispersive (i.e., Q dependent), causing the dielectric tensor Eq. (50) to also become dispersive, the screening is gradually increasing, and the longitudinal exciton-polariton formation occurs, which is expected to be dispersive. However, from Fig. 9(b) it is obvious that dispersivity of exciton-polariton at the scale of $Q \sim 0.01 \text{ nm}^{-1}$ (0.0005 a.u.) is still not visible. This above-mentioned dispersivity is attributed to the geometrical effect appearing in the propagator Eq. (49). The exciton dispersion would probably occur at larger wave vectors $Q \sim 1/a$ when quantum-mechanical dispersivity of conductivity tensor Eqs. (40)–(44) occurs (σ_{μ} becomes Q dependent, the exciton gets kinetic energy, etc.). However, this leads to additional complications that go beyond the scope of this paper. Here we can conclude that the hybridization between 2D transverse excitons and free photons is quite weak and a stronger coupling may be achieved if the phosphorene is in the presence of a more confined electromagnetic field such as those produced by microcavity devices. A theoretical attempt to explain the exciton-polaritons in TMDs is given in Ref. [10]. The hybridization between excitons in various TMDs and in microcavity electromagnetic modes has already been experimentally observed [3,8,9,11].

C. Plasmon-polaritons

Here we present the intraband and interband RPA($G_0^{0,\text{dop}}$) conductivities, the effective number of charge carriers Eq. (42), and the appearance of anisotropic plasmon-polaritons in pristine and doped phosphorene.

Figures 10(a) and 10(b) show the RPA($G_0^{0,\text{dop}}$) optical conductivities $\sigma_{xx}(\omega)$ and $\sigma_{yy}(\omega)$ in doped phosphorene for various electron concentrations: $n = 0$ (black), $n = 5 \times 10^{12} \text{ cm}^{-2}$ (magenta), $n = 10^{13} \text{ cm}^{-2}$ (blue), $n = 5 \times 10^{13}$

cm^{-2} (green), $n = 10^{14} \text{ cm}^{-2}$ (red). The interband contribution σ_x^{inter} in pristine phosphorene ($n = 0$) shows a characteristic onset which consists of a well-defined asymmetric peak at $\omega \approx E_g$. This onset corresponds to $p_x \rightarrow p_x^*$ interband electron-hole excitations. At higher energies, namely, at $\omega \approx 4 \text{ eV}$, another peak appears which corresponds to $p_y \rightarrow p_y^*$ interband electron-hole excitations, as seen in Fig. 5. When the electron concentration n increases, the first peak $p_x \rightarrow p_x^*$ decreases and moves toward higher energies. As already discussed in Sec. III A, this is a consequence of Pauli blocking, i.e., injected electrons occupy the bottom of the conductive band in the interval $E_F - E_C$ (as can be seen in Fig. 5), which reduces the contribution of the direct interband electron-hole excitations in the energy interval $E_g < \omega < E_g + 2(E_F - E_C)$, resulting in a blueshift of the peak of approximately $2(E_F - E_C)$. The second peak $p_y \rightarrow p_y^*$ also decreases with doping, however, it is redshifted. The interband contribution to conductivity σ_y shows the lack of a strong peak at $\omega \approx E_g$. This is expected, considering that the y polarized light is not able to excite direct $p_x \rightarrow p_x^*$ excitations. The first steplike onset at $\omega \approx 3.7 \text{ eV}$ corresponds to $p_y \rightarrow p_x^*$, and the second steplike onset at $\omega \approx 4 \text{ eV}$ corresponds to the already mentioned $p_y \rightarrow p_y^*$ transitions. These onsets weakly depend on doping; the first onset slightly increases and redshifts, while the second one decreases and blueshifts. The intraband/Drude conductivity $\sigma_{\mu}^{\text{intra}}$ depends on the effective number of charge carriers $n_{\mu}^{e,h}$ [see Eq. (42)], which depends on the concentration of injected holes $n < 0$ or electrons $n > 0$ in the semiconductor. The effective number of charge carriers $n_{\mu}^{e,h}$, as shown later, finally defines the intensity of the plasmon-polariton. The left panels in Figs. 10(a) and 10(b) show how the increase of the excess electrons $n > 0$ results in the increase of the Drude conductivities $\sigma_{x,y}$. Also, the Drude conductivity σ_y is, for the same concentration n , smaller than the Drude conductivity σ_x .

To analyze intraband conductivities $\sigma_{x,y}^{\text{intra}}$ quantitatively, in Table II we list the effective concentrations of electrons and

TABLE II. Effective concentrations of holes n_μ^h and electrons n_μ^e as well as Fermi energies E_F relative to the valence E_V or the conduction E_C bands in doped phosphorene. The results are shown as a function of the doping concentration n , where $n < 0$ corresponds to hole doping and $n > 0$ corresponds to electron doping. The temperature is chosen to be $T = 284$ K.

Holes			
n [cm ⁻²]	n_x^h [$10^{-3}a_0^{-2}$]	n_y^h [$10^{-3}a_0^{-2}$]	$E_F - E_V$ [meV]
-1×10^{14}	14	1.9	-339.6
-5×10^{13}	8.8	0.83	-165.8
-1×10^{13}	2.2	0.125	-18.5
-5×10^{12}	1.1	0.059	7.1
Electrons			
n [cm ⁻²]	n_x^e [$10^{-3}a_0^{-2}$]	n_y^e [$10^{-3}a_0^{-2}$]	$E_F - E_C$ [meV]
5×10^{12}	1.1	0.12	18.7
1×10^{13}	2.1	0.25	52.2
5×10^{13}	8	1.1	254
1×10^{14}	12	2.5	445

hole $n_x^{e,h}$ (second column) and $n_y^{e,h}$ (third column) for various doping concentrations n (first column). The convention used here is $n < 0$ if the sample is doped by holes, and $n > 0$ if the sample is doped by electrons. The $n_\mu^{e,h}$ ($\mu = x, y$) are calculated using Eq. (42), and the temperature is chosen to be $T = 284$ K. The fourth column shows the Fermi energy (E_F) in the doped sample relative to E_V (if $n < 0$) or E_C (if $n > 0$).

The decrease of excess holes ($n < 0$) causes a decrease of the effective concentration of holes n_x^h , and an increase of injected electrons ($n > 0$) causes an increase of the effective concentration of electrons n_x^e , noting a symmetrical increase of concentrations n_x^h and n_x^e with respective increases in the concentrations $n < 0$ and $n > 0$, especially for small concentrations $|n|$. A somewhat different behavior applies to concentrations n_y^h and n_y^e . These concentrations are (as also anticipated from Drude conductivities in Fig. 10) more than ten times smaller than concentrations $n_x^{h,e}$. Also, the property of symmetrical increase is here violated, so the concentration n_y^e increases about twice as fast relative to the concentration n_y^h (for smaller $|n|$). The effective concentrations $n_\mu^{e,h}$ define the intensity and frequency of collective modes arising due to hybridization between longitudinal 2D plasmons and photons, called plasmon-polaritons.

Figures 11(a)–11(d) show the real part of the screened conductivities $\text{Re } \sigma_{xx}^{\text{scr}}$ and $\text{Re } \sigma_{yy}^{\text{scr}}$ for momentum transfers Q_x and Q_y , respectively, in doped phosphorene as a function of excess electron concentrations, namely, (a) $n = 5 \times 10^{12}$ cm⁻², (b) $n = 1 \times 10^{13}$ cm⁻², (c) $n = 5 \times 10^{13}$ cm⁻², and (d) $n = 1 \times 10^{14}$ cm⁻². Momentum transfer Q_y is here presented as a negative wave vector ($Q < 0$). The polarization of induced currents is collinear with the direction of propagation and therefore Figs. 11(a)–11(d) represent the intensities of longitudinal p(TM) electromagnetic modes, i.e., 2D plasmon-polaritons 2D-PP_x and 2D-PP_y. We emphasize that the frequency scale here is in THz. Only the intraband conductivity $\sigma_\mu^{\text{intra}}$, or more precisely the effective numbers of charge carriers, determine the energy and the intensity of the

2D-PP_μ. Therefore, following Eq. (50), the intense patterns seen in Figs. 11(a)–11(d) follow the zeros of the dielectric functions

$$\epsilon_{\mu\mu}(Q\hat{\mu}, \omega) = 1 + \frac{2\pi\beta L}{\omega} \sigma_\mu^{\text{intra}}(\omega); \quad \mu = x, y. \quad (56)$$

Consequently, the σ^{inter} and σ^{ladd} do not affect plasmon-polaritons. As expected, by increasing the doping concentration $n > 0$ and the concurrent increase in n_μ^e , 2D-PP_μ become more intense and rise in energy. Also, the anisotropy in the effective concentrations $n_x^e > n_y^e$ is reflected in the anisotropy of 2D-PP_μ propagation, such that the 2D-PP_x has larger energy and is more intense than 2D-PP_y for a given momentum value. It can be noticed that 2D-PP_μ only retains a polaritonlike character (follows the light line Qc) at very small frequencies, soon after following the standard square-root-like 2D plasmon. However, the polaritonlike character increases gradually with doping n , so, for example, for dopings $n = 1.0^{13}$ cm⁻², $n = 5.0^{13}$ cm⁻², and $n = 10^{14}$ cm⁻² the 2D-PP_x behaves as a polariton up to $\omega < 0.5$ THz, $\omega < 1.0$ THz, and $\omega < 2.0$ THz, respectively. Besides following the light line Qc for very small ω , 2D-PP_x merges with the continuum of radiative electromagnetic modes, the blue pattern at $\omega > Qc$ that is most noticeable in Fig. 11(d). The merging with the continuum of radiative modes is considerably weaker for the y polarized plasmon-polariton. Here we can conclude that even a small fraction of the excess electrons in the phosphorene conduction band, ranging from $n \sim 5 \times 10^{12} - 2 \times 10^{13}$ cm⁻² ($E_F - E_C \sim 19 - 108$ meV) leads to a significant manipulation of the anisotropic plasmon-polariton intensity and energy.

IV. CONCLUSIONS

We have developed a formalism suitable for studying electromagnetic modes in a wide class of conducting and semiconducting 2D materials. Our method properly accounts for the electron-hole interaction and the corresponding exciton-polariton effects as well as for the screened electromagnetic collective modes such as plasmon polaritons. The approach is completely equivalent to the widely used TD-SHF approach, with additional benefits such as separability of the screening RPA and the ladder (electron-hole interaction) terms as well as inclusion of the polariton effects (photon-matter interaction). The formulation can easily be adapted to calculate the electromagnetic modes in 2D van der Waals heterostructures or to calculate the interaction of these modes within confined cavity modes. Here the formulation was applied to calculate the optical conductivity (the evolution of the exciton intensity and binding energy) in doped phosphorene. We have clearly demonstrated the mechanisms of exciton quenching (sudden drop of the exciton binding energy and intensity) due to injection of electrons in the phosphorene conduction band. Further, the formulation is applied to calculate the interaction of the phosphorene transverse exciton with free photons, where we have observed a weak hybridization and exciton-polariton formation. Finally, the method was applied to demonstrate the tuning of anisotropic plasmon-polaritons in phosphorene by electron doping.

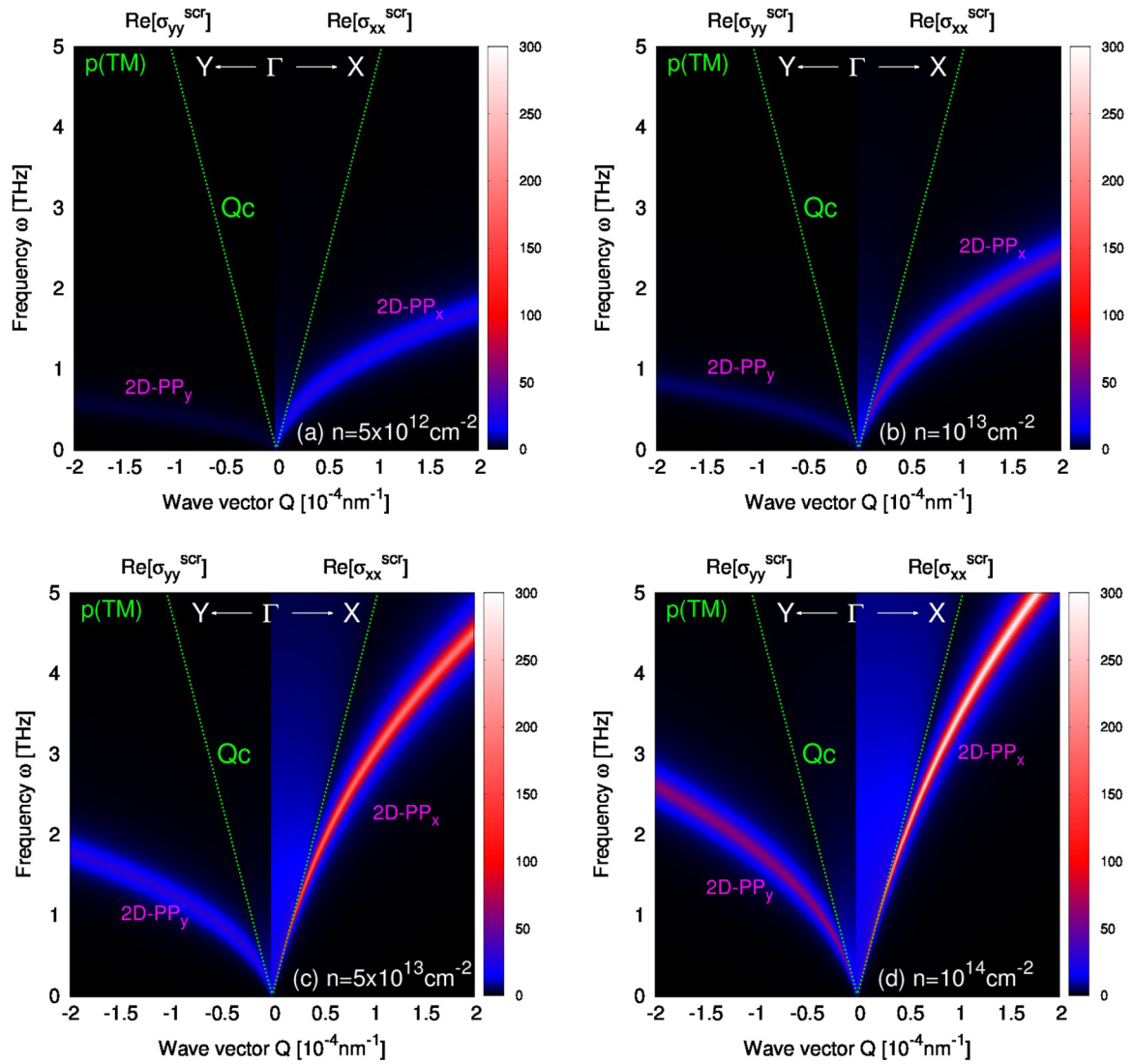


FIG. 11. Real part of the screened conductivities σ_{xx}^{scr} and σ_{yy}^{scr} for momentum transfer $\mathbf{Q} = Q_x \mathbf{x}$ and $\mathbf{Q} = Q_y \mathbf{y}$, respectively, as a function of doping concentrations: (a) $n = 5 \times 10^{12} \text{ cm}^{-2}$, (b) $n = 1 \times 10^{13} \text{ cm}^{-2}$, (c) $n = 5 \times 10^{13} \text{ cm}^{-2}$, and (d) $n = 1 \times 10^{14} \text{ cm}^{-2}$. Panels show the intensities of longitudinal p(TM) electromagnetic modes in the THz frequency region, i.e., the 2D plasmon polaritons 2D-PP_x and 2D-PP_y.

ACKNOWLEDGMENTS

V.D. acknowledges financial support from the Croatian Science Foundation (Grant No. IP-2020-02-5556) and European Regional Development Fund for the QuantiXLie Centre of Excellence (Grant No. KK.01.1.1.01.0004). D.N. additionally acknowledges financial support from the Croatian Science Foundation (Grant No. UIP-2019-04-6869) and from the European Regional Development Fund for the Center

of Excellence for Advanced Materials and Sensing Devices (Grant No. KK.01.1.1.01.0001). Computational resources were provided by the Donostia International Physics Center (DIPC) computing center as well as from the Imbabura cluster of Yachay Tech University, which was purchased under Contract No. 2017-024 (SIE-UIITEY-007-2017). V.D. thank Zoran Mišković for useful discussions which also motivated this research.

- [1] A. Chernikov, A. M. van der Zande, H. M. Hill, A. F. Rigosi, A. Velauthapillai, J. Hone, and T. F. Heinz, *Phys. Rev. Lett.* **115**, 126802 (2015).
- [2] O. B. Aslan, M. Deng, and T. F. Heinz, *Phys. Rev. B* **98**, 115308 (2018).
- [3] T. Low, A. Chaves, J. D. Caldwell, A. Kumar, N. X. Fang, P. Avouris, T. F. Heinz, F. Guinea, L. Martin-Moreno, and Frank Koppens, *Nat. Mater.* **16**, 182 (2017).
- [4] Y. Li, A. Chernikov, X. Zhang, A. Rigosi, H. M. Hill, A. M. van der Zande, D. A. Chenet, En-Min Shih, J. Hone, and T. F. Heinz, *Phys. Rev. B* **90**, 205422 (2014).
- [5] A. Ramasubramaniam, *Phys. Rev. B* **86**, 115409 (2012).
- [6] T. Mueller and E. Malic, *npj 2D Mater. Appl.* **2**, 29 (2018).
- [7] Y. Lin, X. Ling, L. Yu, S. Huang, Allen L. Hsu, Yi-Hsien Lee, J. Kong, M. S. Dresselhaus, and T. Palacios, *Nano Lett.* **14**, 5569 (2014).

- [8] X. Liu, T. Galfsky, Z. Sun, F. Xia, E.-c. Lin, Y.-H. Lee, S. Kéna-Cohen, and V. M. Menon, *Nat. Photonics* **9**, 30 (2015).
- [9] S. Dufferwiel, T. P. Lyons, D. D. Solnyshkov, A. A. P. Trichet, A. Catanzaro, F. Withers, G. Malpuech, J. M. Smith, K. S. Novoselov, M. S. Skolnick, D. N. Krizhanovskii, and A. I. Tartakovskii, *Nat. Commun.* **9**, 4797 (2018).
- [10] Y. N. Gartstein, Xiao Li, and C. Zhang, *Phys. Rev. B* **92**, 075445 (2015).
- [11] J. B. Khurgin, *Optica* **2**, 740 (2015).
- [12] A. Krasnok, S. Lepeshov, and A. Alú, *Optic Express* **26**, 15972 (2018).
- [13] R. Petersen, T. G. Pedersen, and F. Javier García de Abajo, *Phys. Rev. B* **96**, 205430 (2017).
- [14] A. Agarwal, M. S. Vitiello, L. Viti, A. Cupolillo, and A. Politano, *Nanoscale* **10**, 8938 (2018).
- [15] R. E. Groenewald, M. Rösner, G. Schönhoff, S. Haas, and T. O. Wehling, *Phys. Rev. B* **93**, 205145 (2016).
- [16] Y. Xu, C.-Y. Hsieh, L. Wu, and L. K. Ang, *J. Phys. D: Appl. Phys.* **52**, 065101 (2019).
- [17] Q. Ouyang, S. Zeng, Li Jiang, Junle Qu, Xuan-Quyen Dinh, Jun Qian, Sailing He, Philippe Coquet, and Ken-Tye Yong, *J. Phys. Chem. C* **121**, 6282 (2017).
- [18] A. Nemilentsau, T. Low, and G. Hanson, *Phys. Rev. Lett.* **116**, 066804 (2016).
- [19] E. van Veen, A. Nemilentsau, A. Kumar, R. Roldán, M. I. Katsnelson, T. Low, and S. Yuan, *Phys. Rev. Appl.* **12**, 014011 (2019).
- [20] D. A. Prishchenko, V. G. Mazurenko, M. I. Katsnelson, and A. N. Rudenko, *2D Mater.* **4**, 025064 (2017).
- [21] F. G. Ghamsari and R. Asgari, *Plasmonics* **15**, 1289 (2020).
- [22] V. A. Margulis and E. E. Muryumin, *Phys. Rev. B* **98**, 165305 (2018).
- [23] V. A. Margulis, E. E. Muryumin, and E. A. Gaiduk, *J. Opt.* **18**, 055102 (2016).
- [24] D. T. Debu, S. J. Bauman, D. French, H. O. H. Churchill, and J. B. Herzog, *Sci. Rep.* **8**, 3224 (2018).
- [25] T. Low, A. S. Rodin, A. Carvalho, Y. Jiang, H. Wang, F. Xia, and A. H. Castro Neto, *Phys. Rev. B* **90**, 075434 (2014).
- [26] H. T. Nguyen-Truong, *J. Mater. Sci.* **53**, 15541 (2018).
- [27] B. Ghosh, P. Kumar, A. Thakur, Y. S. Chauhan, S. Bhowmick, and A. Agarwal, *Phys. Rev. B* **96**, 035422 (2017).
- [28] F. Ferreira and R. M. Ribeiro, *Phys. Rev. B* **96**, 115431 (2017).
- [29] C. E. P. Villegas, A. S. Rodin, A. C. Carvalho, and A. R. Rocha, *Phys. Chem. Chem. Phys.* **18**, 27829 (2016).
- [30] K. Lyon, M. R. Preciado-Rivas, C. Zamora-Ledezma, V. Despoja, and D. J. Mowbray, *J. Phys.: Condens. Matter* **32**, 415901 (2020).
- [31] S. Arra, R. Babar, and M. Kabir, *Phys. Rev. B* **99**, 045432 (2019).
- [32] L. Seixas, A. S. Rodin, A. Carvalho, and A. H. Castro Neto, *Phys. Rev. B* **91**, 115437 (2015).
- [33] A. S. Rodin, A. Carvalho, and A. H. Castro Neto, *Phys. Rev. B* **90**, 075429 (2014).
- [34] J.-H. Lin, H. Zhang, and X.-L. Cheng, *Front. Phys.* **10**, 1 (2015).
- [35] R. Tian, R. Fei, S. Hu, T. Li, B. Zheng, Y. Shi, J. Zhao, L. Zhang, X. Gan, and X. Wang, *Phys. Rev. B* **101**, 235407 (2020).
- [36] X. Wang, A. M. Jones, K. L. Seyler, V. Tran, Y. Jia, H. Zhao, H. Wang, L. Yang, X. Xu, and F. Xia, *Nat. Nanotechnol.* **10**, 517 (2015).
- [37] J. Yang, R. Xu, J. Pei, Y. W. Myint, F. Wang, Z. Wang, S. Zhang, Z. Yu, and Y. Lu, *Light Sci. Appl.* **4**, e312 (2015).
- [38] L. Li, J. Kim, C. Jin, G. Jun Ye, D. Y. Qiu, F. H. da Jornada, Z. Shi, L. Chen, Z. Zhang, F. Yang, K. Watanabe, T. Taniguchi, W. Ren, S. G. Louie, X. Hui Chen, Y. Zhang, and F. Wang, *Nat. Nanotechnol.* **12**, 21 (2017).
- [39] L. Hedin, *Phys. Rev.* **139**, A796 (1965).
- [40] W. Hanke and L. J. Sham, *Phys. Rev. Lett.* **43**, 387 (1979).
- [41] W. Hanke and L. J. Sham, *Phys. Rev. B* **21**, 4656 (1980).
- [42] G. Strinati, *Phys. Rev. B* **29**, 5718 (1984).
- [43] M. S. Hybertsen and S. G. Louie, *Phys. Rev. B* **34**, 5390 (1986); M. Rohlfing and S. G. Louie, *Phys. Rev. Lett.* **81**, 2312 (1998).
- [44] M. Rohlfing and S. G. Louie, *Phys. Rev. Lett.* **83**, 856 (1999).
- [45] M. Rohlfing and S. G. Louie, *Phys. Rev. B* **62**, 4927 (2000).
- [46] G. Onida, L. Reining, and A. Rubio, *Rev. Mod. Phys.* **74**, 601 (2002).
- [47] J. Yan, K. W. Jacobsen, and K. S. Thygesen, *Phys. Rev. B* **86**, 045208 (2012).
- [48] D. Y. Qiu, F. H. da Jornada, and S. G. Louie, *Phys. Rev. Lett.* **111**, 216805 (2013).
- [49] J. Koskelo, G. Fugallo, M. Hakala, M. Gatti, F. Sottile, and P. Cudazzo, *Phys. Rev. B* **95**, 035125 (2017).
- [50] F. Huser, T. Olsen, and Kristian S. Thygesen, *Phys. Rev. B* **87**, 235132 (2013).
- [51] A. Molina-Sanchez, D. Sangalli, K. Hummer, A. Marini, and L. Wirtz, *Phys. Rev. B* **88**, 045412 (2013).
- [52] V. Despoja, M. Šunjić, and L. Marušić, *Phys. Rev. B* **80**, 075410 (2009).
- [53] D. Novko, M. Šunjić, and V. Despoja, *Phys. Rev. B* **93**, 125413 (2016).
- [54] G. D. Mahan, *Many-particle Physics*, 3rd ed. (Plenum Press, New York, 1990).
- [55] S. Ponce, F. Macheda, E. R. Margine, N. Marzari, N. Bonini, and F. Giustino, *arXiv:2105.04192*.
- [56] P. Giannozzi, S. Baroni, N. Bonini, M. Calandra, R. Car, C. Cavazzoni, D. Ceresoli, G. L. Chiarotti, M. Cococcioni, I. Dabo *et al.*, *J. Phys.: Condens. Matter* **21**, 395502 (2009).
- [57] N. Troullier and J. L. Martins, *Phys. Rev. B* **43**, 1993 (1991).
- [58] J. P. Perdew, K. Burke, and M. Ernzerhof, *Phys. Rev. Lett.* **77**, 3865 (1996).
- [59] H. J. Monkhorst and J. D. Pack, *Phys. Rev. B* **13**, 5188 (1976).
- [60] J. J. Mortensen, L. B. Hansen, and K. W. Jacobsen, *Phys. Rev. B* **71**, 035109 (2005).
- [61] J. Enkovaara, C. Rostgaard, J. J. Mortensen, J. Chen, M. Dulak, L. Ferrighi, J. Gavnholt, C. F. Glinsvad, V. Haikola, H. A. Hansen, H. H. Kristoffersen, M. Kuisma, A. H. Larsen, L. Lehtovaara, M. Ljungberg, O. Lopez-Acevedo, P. G. Moses, J. Ojanen, T. Olsen, V. Petzold, N. A. Romero *et al.* *J. Phys.: Condens. Matter* **22**, 253202 (2010).
- [62] D. Van Tuan, B. Scharf, I. Žutić, and H. Dery, *Phys. Rev. X* **7**, 041040 (2017).